

# **Signal Optimization for Unilateral NMR Magnet Design**

by

**Hershel Caytak**

B.Sc, Jerusalem College of Technology, 2009

A thesis submitted to the Faculty of Graduate and Postdoctoral  
Affairs in partial fulfillment of the requirements for the degree of

**Master of Applied Science in Biomedical Engineering**

Ottawa-Carleton Institute for Biomedical Engineering  
Department of Systems and Computer and Engineering  
Carleton University

Ottawa, Ontario, Canada, K1S 5B6

September 2011

© Copyright 2011 Hershel Caytak



Library and Archives  
Canada

Published Heritage  
Branch

395 Wellington Street  
Ottawa ON K1A 0N4  
Canada

Bibliothèque et  
Archives Canada

Direction du  
Patrimoine de l'édition

395, rue Wellington  
Ottawa ON K1A 0N4  
Canada

*Your file* *Votre référence*  
*ISBN: 978-0-494-83064-2*  
*Our file* *Notre référence*  
*ISBN: 978-0-494-83064-2*

#### NOTICE:

The author has granted a non-exclusive license allowing Library and Archives Canada to reproduce, publish, archive, preserve, conserve, communicate to the public by telecommunication or on the Internet, loan, distribute and sell theses worldwide, for commercial or non-commercial purposes, in microform, paper, electronic and/or any other formats.

The author retains copyright ownership and moral rights in this thesis. Neither the thesis nor substantial extracts from it may be printed or otherwise reproduced without the author's permission.

---

In compliance with the Canadian Privacy Act some supporting forms may have been removed from this thesis.

While these forms may be included in the document page count, their removal does not represent any loss of content from the thesis.

#### AVIS:

L'auteur a accordé une licence non exclusive permettant à la Bibliothèque et Archives Canada de reproduire, publier, archiver, sauvegarder, conserver, transmettre au public par télécommunication ou par l'Internet, prêter, distribuer et vendre des thèses partout dans le monde, à des fins commerciales ou autres, sur support microforme, papier, électronique et/ou autres formats.

L'auteur conserve la propriété du droit d'auteur et des droits moraux qui protègent cette thèse. Ni la thèse ni des extraits substantiels de celle-ci ne doivent être imprimés ou autrement reproduits sans son autorisation.

---

Conformément à la loi canadienne sur la protection de la vie privée, quelques formulaires secondaires ont été enlevés de cette thèse.

Bien que ces formulaires aient inclus dans la pagination, il n'y aura aucun contenu manquant.

  
**Canada**

The undersigned recommend to  
the Faculty of Graduate and Postdoctoral Affairs  
acceptance of the thesis

**Signal Optimization for Unilateral NMR Magnet Design**

submitted by

**Hershel Caytak, B.Sc.**

in partial fulfillment of the requirements for the degree of

**Master of Applied Science in Biomedical Engineering**

---

Andrew Marble, Thesis Supervisor

---

Chair, Howard Schwartz, Department of Systems and Computer Engineering

## **Abstract**

In this thesis, we propose a method of signal optimization for an adjustable unilateral NMR (nuclear magnet resonance) permanent magnet design. Unilateral NMR magnets have many advantages over the conventional MRI (magnetic resonance imaging) bore design, including mobility, cost and open access geometry, but have not been adopted on a large scale for use in major fields varying from medical to industrial applications due to limitations such as poor SNR (signal noise ratio), low static magnetic field strength and field inhomogeneities. Attempts to improve these parameters have shown that a tradeoff occurs, i.e. increasing field strength reduces field homogeneity and vice versa. We introduce a model of a simple NMR magnet design where field strength and homogeneity can be controlled by an adjustable central magnet shim unit. We derive analytical expressions that are used to model the experimental sensitivity as a function of magnet geometry. We then present experimental data of a physical prototype of the model design that supports simulation results. In addition we show that field homogeneity is a more dominant factor in SNR optimization than field strength, perhaps indicating the future direction of unilateral magnet design.

## **Acknowledgements**

I would like to thank my supervisor, Dr. Andrew Marble, for his invaluable guidance and support throughout the course of my studies. I feel that I have been given the right balance of assistance and independence to allow me to express my potential to the fullest. I would like to acknowledge my colleague, Gabriel Seyoum. The discussions we had were most beneficial in introducing me to the world of NMR research.

I would like to express my gratitude to my parents for their support and encouragement.

Last but not least, I would like to thank my wife Aliza, for her patience and support during my challenging years of study.

## Table of Contents

<b>Abstract</b> .....	<b>iii</b>
<b>Acknowledgements</b> .....	<b>iv</b>
<b>Table of Contents</b> .....	<b>v</b>
<b>List of Tables</b> .....	<b>ix</b>
<b>List of Figures</b> .....	<b>ix</b>
<b>List of Abbreviations</b> .....	<b>xii</b>
<b>List of Symbols</b> .....	<b>xiii</b>
<b>1 Introduction</b> .....	<b>1</b>
1.1 Research Motivation .....	<b>1</b>
1.2 Research Objectives.....	<b>3</b>
1.3 Thesis Organization .....	<b>5</b>
<b>2 Background</b> .....	<b>6</b>
2.1 Magnetic Resonance .....	<b>6</b>
2.1.1 Net Magnetization of Atomic Nuclei.....	<b>6</b>
2.1.2 Free Induction Decay .....	<b>10</b>
2.1.3 $T_1$ Relaxation.....	<b>11</b>
2.1.4 $T_2$ and $T_2^*$ Relaxation .....	<b>11</b>
2.1.5 Hahn Echo.....	<b>13</b>
2.1.6 Carr-Purcell-Meiboom-Gill Pulse Sequence .....	<b>13</b>

2.2 System Hardware Components of NMR Magnets.....	14
2.2.1 $B_0$ Field .....	14
2.2.1 $B_1$ Field .....	16
2.2.2 Signal Generation and Processing .....	17
<b>3 Literature Review .....</b>	<b>18</b>
3.1 Analysis of Open Geometry Mobile NMR Magnet Designs.....	18
3.1.1 Homogeneous Field Designs .....	19
3.1.1.1 Jackson Geometry .....	19
3.1.1.2 Schlumberger and Numar Designs .....	21
3.1.1.3 Unilateral NMR Permanent Magnet Designs .....	23
3.1.2 Inhomogeneous Field Designs.....	27
3.1.2.1 NMR-MOUSE .....	28
3.2 Field Homogeneity vs. Field Strength .....	30
3.3 Conclusion .....	32
<b>4 Model Simulation .....</b>	<b>33</b>
4.1 Model Description .....	33
4.2 Signal Optimization .....	34
4.2.1 Calculation of Maximum Signal Density .....	35
4.2.2 $B_0$ Field Simulation.....	38
4.2.3 $B_1$ Field Simulation.....	42
4.2.4 Calculation of $B_{1n}$ .....	45

4.2.5 Setting Evaluation Window Boundaries.....	46
4.2.6 Determination of Center Bandwidth Frequencies.....	50
4.2.7 Simulation Algorithm Flow .....	54
4.3 Results.....	55
4.4 Conclusion .....	57
<b>5 Experimental Methods .....</b>	<b>58</b>
5.1 Prototype Design.....	58
5.2 Experimental Design.....	59
5.3 NMR System Hardware and Software.....	61
5.3.1 Bruker Minispec Pulse Sequence Parameters.....	62
5.4 Signal Measurement.....	62
5.4.1 1D Field Scanning.....	63
5.4.2 RF Coil Tuning and Matching .....	68
5.4.3 CPMG Pulse Sequence .....	71
5.4.4 Maximum Signal Amplitude Measurements .....	72
5.5 Results.....	74
5.6 Conclusion .....	75
<b>6 Conclusions and Future Studies .....</b>	<b>77</b>
6.1 Conclusions.....	77
6.2 Summary of Contributions.....	77
6.3 Future Work.....	78
<b>References.....</b>	<b>79</b>

## **List of Tables**

5.1 A table of homogeneous region location and frequency vs. magnet offsets is shown for results derived from field scanning with a VXM Stepping Motor Controller. ....	<b>82</b>
---	-----------

## List of Figures

2.1 Reproduced from [15]. A vector representation of the precession of a magnetic moment around the z-axis of the $B_0$ field is illustrated. ....	22
2.2 Reproduced from [22]. The CPMG pulse sequence consists of an initial $90^\circ$ excitation pulse, a period $\tau$ and a $180^\circ$ pulse and an echo after a subsequent $\tau$ period. .	28
3.1 Reproduced from [27]. The “Jackson Geometry” generates a homogeneous toroidal field region through employing two opposed cylinder magnets at a fixed distance from a radial axis/plane. ....	35
3.2 Reproduced from [38]. Concentric “shells” of sensitive volumes generated by choosing excitation frequencies to spatially select slices of variable field strength.....	36
3.3 Reproduced from [38].The general scheme of the Schlumberger PNMT device is shown consisting of bar magnets that generate a homogeneous strong field and a RF coil designed to excite the sample. ....	37
3.4 Reproduced from [55]. (a)-(c) Different magnet configurations used to generate remote homogeneous fields.. ....	41
3.5 Reproduced from [55]. The basic design of the NMR-MOUSE consists of two permanent magnets with anti-parallel magnetization and a RF coil.....	43
4.1 A 2D NMR magnet model representation based on the Marble et al. design [47] is shown along a y and z axis. ....	48
4.2 The upper surface of the magnet is centered under the origin of the y and z axis. ....	52
4.3 Reproduced from [47]. The bar magnet can be represented by two sheets of current composed of infinitely deep line current element of width $dz'$ . ....	53

4.4 <b>A</b> . The contour map of the $ B_0 $ field is shown for a central magnet offset of -6 mm.	<b>55</b>
4.5 The direction of a normalized vector field is shown for <b>A</b> the magnet array $B_0$ field and <b>B</b> the RF coil loop $B_1$ field.	<b>58-59</b>
4.6 Reproduced from [67]. The orientation of the $B_0$ and $B_1$ fields are shown.	<b>59</b>
4.7 The direction of the normalized $B_{1n}$ vector field is shown.	<b>61</b>
4.8 A schematic diagram is shown of the magnet configuration used to calculate the NMR signal.	<b>62</b>
4.9 1D profiles of a central slice of the $B_0$ field. <b>A</b> at -4 mm displacement and <b>B</b> at -7 mm.	<b>63-64</b>
4.10 <b>A – D</b> Center bandwidth frequency values are shown with their corresponding bandwidth.	<b>65-67</b>
4.11 The center bandwidth frequencies are shown for zeroed first and second order field derivatives vs. central magnet displacements.	<b>68</b>
4.12 The basic stages of the simulation algorithm are illustrated; simulation of the $B_0$ , $B_1$ , $B_{1n}$ field, calculation of $S_{max}$ , central magnet displacement and plotting $S_{max}$ vs. displacement.	<b>69</b>
4.13 The percentage of maximum signal density at .6 mm increments is plotted vs. displacement. <b>A</b> . for a constant $B_{1n}$ and <b>B</b> for a RF coil $B_{1n}$ .	<b>70-71</b>
5.1 Single-sided magnet array in metal housing. The central adjustable magnet is shown with an offset.	<b>74</b>
5.2 Experimental design: The oil sample is contained in a cylindrical container stabilized above the center of the magnet array by a wooden dowel attached to VXM Stepping Motor Controller.	<b>75</b>

5.3 The Bruker Optics NMR spectrometer hardware includes (right) RF pulse generator and (left –back) a signal preamplifier. ....	<b>76</b>
5.4 The 1D field profiles of <b>A</b> -9 mm , <b>B</b> -6mm, <b>C</b> -5 mm <b>D</b> -4mm <b>E</b> -3 mm and <b>F</b> 0 mm displacements are shown .....	<b>78-81</b>
5.5 <b>A.</b> Reproduced from [69]. The resonant circuit consists of an inductance coil and variable capacitors in series and in parallel. <b>B.</b> Soldered capacitors in series and in parallel determine the resonant frequency of the circuit.....	<b>84</b>
5.6 Simulation and experimental results are compared for <b>A.</b> Distance of center bandwidth from the magnet surface vs. displacement and <b>B.</b> bandwidth center frequencies vs. displacement. ....	<b>85-86</b>
5.7 A plot of the T2 decay of oil for a 64 echo CPMG train <b>A.</b> for -5 mm and <b>B.</b> -6 mm where each peak represents one echo. ....	<b>88-89</b>
5.8 The simulation and experimental results of maximum signal density vs. displacement are compared. ....	<b>90</b>
5.9 A plot showing maximum signal density, field homogeneity and field strength vs. displacement. ....	<b>91</b>

## List of Abbreviations

A/D	Analog to Digital
A.U.	Arbitrary Units
CPMG	Carr-Purcell-Meiboom-Gill
FID	Free Induction Decay
FWHM	Full-Width Half -Maximum
HALO	High Access Low Oersted
MOLE	Mobile Lateral Explorer
MOUSE	MOBILE Universal Surface Explorer
MR	Magnetic Resonance
MRI	Magnetic Resonance Imaging
MRIL	Magnetic Resonance Imaging Logging
NdFeB	Neodymium Iron Boron
NMR	Nuclear Magnetic Resonance
PNMT	Pulse Nuclear Magnetism Tool
PPM	Parts Per Million
RF	Radiofrequency
SmCo	Samarium-Cobalt
Smax	Maximum Signal Density
SNR	Signal-to-Noise Ratio

## List of Symbols

$\cdot$	Dot product
$ \cdot $	Absolute value of $\cdot$
$\vec{B}$	Magnetic Field Vector
$B_0$	Static Magnetic Field
$\Delta B_0$	Magnetic Field Inhomogeneity
$B_1$	RF Magnetic Field
$B_{1xy}$	RF Field in the $xy$ plane
$B_{1n}$	Components of $B_1$ orthogonal to $B_0$
$C$	Capacitance [Farad]
$C_{1,2}(t)$	Time Dependent Density Operator Coefficients
$e$	Base of natural Logarithm
$F(\Delta\omega_0)$	System Frequency Response
$\Phi$	RF Pulse Phase
$\gamma$	Gyromagnetic Ratio
$^1H$	Hydrogen
$h$	Plank's Constant
$H_r$	Magnetic Field Radial Component
$I$	Quantum Spin
$i$	Current in Amperes
$k$	Boltzmann's Constant
$\mu$	Magnetic Moment
$\mu_0$	Permeability of Free Space
$L$	Inductance [Henry]
$\vec{M}$	Magnetization
$M_0$	Net Magnetization Vector
$M_{xy}$	$xy$ Component of $M_0$
$N_\alpha$	Spin Population at Lower Energy State

$N_{\beta}$	Spin Population at Higher Energy State
Rx	Receive Coils
$\rho(t)$	Time Dependent Density Operator
$t$	Temperature [K]
$T_1$	Longitudinal Relaxation Time
$T_2$	Transverse Relaxation Time
$T_{2m}$	Dephasing due to Field Inhomogeneities
$T_{2ms}$	Dephasing due to Inhomogeneous Sample Magnetic Susceptibilities
$\tau$	Pulse Sequence Delay
T	Tesla
Tx	Transmit Coils
TxRx	Transmit/Receive Coils
$\vartheta$	Angle of Rotation With Respect to the Z-axis
$\omega_o$	Resonant Frequency
$\omega_{1(r)}$	RF Frequency at Point r
$\chi$	Nuclear Magnetic Susceptibility
$\hat{y} \hat{z}$	Unit Vectors in Cartesian Coordinates
$\hat{\theta}'$	Unit Normal of an Angle in Polar Coordinates
$\Omega$	Resistance [Ohm]

# 1 Introduction

## 1.1 Research Motivation

Discovery of the principles of Magnetic Resonance can be dated back to 1938 when the nuclear magnetic resonance of molecular beams was described and measured by Isador Rabi [1]. In 1946 further progress was achieved when Felix Bloch [2] and Edward Mills Purcell [3] independently measured the NMR (Nuclear Magnetic Resonance) properties of liquids and solids respectively. Rabi, Bloch and Purcell discovered that atomic nuclei possessing a *magnetic moment* such as  $^1H$  (or any element with a *non-zero spin*) could absorb and emit RF (Radio Frequency) energy when placed in an external field of a strength specific to the element. They observed that absorption and emission of energy occurred when the *precession* of nuclei – determined by the strength of the polarizing field and the gyromagnetic ratio of the element – were in resonance with the RF wave frequency [1, 2, 3]. Since measurement and observation of magnetic resonance of nuclei can be used to provide chemical and structural information at the atomic and molecular level, development of NMR techniques provided a powerful versatile tool for probing the fundamental properties of matter.

Although less than a decade after the seminal discoveries of Bloch and Purcell's applications of NMR had already been developed for the oil logging industry [4], MRI (Magnetic Resonance Imaging) techniques only began after the pioneering work of Mansfield and Grannell [5] in 1973 and independently of Lauterbur [6]. The advent of MRI scanners provided medical science with a safe non-invasive imaging modality with

significant advantages over other traditional techniques such as X-ray imaging. In practice, significant limitations of conventional MRI systems include high cost, immobility and large power requirements. A self-shielded whole body MRI system may weigh up to 32 tonnes while a non-shielded device may weigh between 6 – 8 tonnes [7]. Large closed bore solenoidal electromagnets have been used traditionally in the design of conventional MRI scanners since they provide the highest homogeneity [8] and field strength [9] over the largest volume, allowing the superior SNR (Signal Noise Ratio) performance and fast scan acquisition time required in medical imaging. The restrictive geometry of this design is however disadvantageous for claustrophobic patients as well as when analysis of samples of large or unusual dimensions are required.

The age of flexible open geometry devices began with inside-out NMR where spectrometers are lowered into bore holes to allow detection and analysis of fluid in the surrounding rock layers, and continued with the development of portable one-sided magnets [4] designed for use in a large range of medical and industrial applications[29,41-43]. The development of portable one-sided permanent magnet magnetic resonance probes removed many of the restrictions and limitations of conventional systems but serious challenges still remained. Due to low static field strength and homogeneity, single sided mobile NMR devices typically have a lower signal sensitivity and spectral resolution than conventional bore shaped magnets [10] offsetting any advantages accrued from the flexible design. Although NMR signal is proportional both to field strength and homogeneity [11], increasing one parameter necessarily results in the reduction of the other, resulting in an inevitable tradeoff. Attempts to improve SNR resulted in 2 classes of devices, the first class focused on

maximizing field strength at the expense of homogeneity while the second prioritized homogeneous field generation at the cost of reduced field strength [12].

One of the problems encountered by researchers in the field of unilateral NMR magnet design is the lack of systematic studies that compare SNR performance achieved from each method. While numerous models have been developed (see section 3) researchers have generally employed an “ad hoc” approach towards building and designing devices without investigating of how to balance the field strength vs. homogeneity tradeoff in terms of maximizing device SNR.

This work attempts to fill this void by investigating the parameter – field strength or homogeneity – that plays a more dominant role in SNR optimization. In addition, the behavior of a simple unilateral NMR magnet design is simulated and a configuration maximizing SNR is determined and validated through experimental methods. It is hoped that this will prove of use to researchers in laying the groundwork for future unilateral NMR magnet design.

## **1.2 Research Objectives**

The objectives of this thesis work were threefold:

- to investigate the singular parameter - field strength or homogeneity – that plays a greater role in maximizing SNR for unilateral permanent magnet devices,
- to accurately model the behavior of a unilateral NMR prototype design and
- to calculate the prototype configuration that generates a maximal NMR signal by optimizing field parameters through simulation and experimental methods.

We intentionally chose to evaluate a simple magnet configuration that trades strength for homogeneity by varying the single parameter of magnet position. The fact that SNR optimization was computed solely for our single magnet design presents some limitations on the achieved results. The unique geometry of each magnet design may preclude any overarching generalizations and conclusions based on the results of this sole analysis. Results achieved from the simulation model are expected to differ from experimental data derived from a physical prototype due to, **a**: the inherent inaccuracies of modeling a 2D slice of a 3D physical prototype, **b**: simplifying assumptions taken in developing the model algorithms such as ignoring the signal evolution during a CPMG (Carr –Purcell-Meiboom-Gill) pulse (see 4.2.4) and **c**: inaccuracies in the various stages of the experimental process, such as coil design and tuning, magnet adjustment and signal acquisition. We note however that a good fit is shown to exist between results of the theoretical model and the experimental prototype (see 5.5 and Fig. 5.8).

Despite these limitations, it is hoped that the conclusions of this research will provide a “proof of concept”, if not for every circumstance then at least for a limited set of cases of similar design. The concept behind the signal optimization is relatively simple and may be applied to other magnet designs. In addition, the results of this work present a significant step towards developing and improving a unilateral magnet design prototype. In conclusion we believe that the work of this thesis represents a significant advance in the field of unilateral NMR magnet design.

### **1.3 Thesis Organization**

Chapter 2 of the thesis introduces some of the basic concepts of NMR including magnetic resonance, Larmor frequency, common NMR measurements and pulse sequences and the basic hardware of conventional and open MR systems.

Chapter 3 provides a survey of existing work in the field of unilateral permanent magnet design. The two basic categories discussed are inhomogeneous and homogeneous field devices. An analysis is given of some of the pros and cons of the designs as well as the relative advantages of our proposed model and method.

Chapter 4 describes the model simulation design and parameters including magnet dimensions, field simulation and bandwidth frequencies. The algorithm flow is discussed with attention to maximum signal density calculation. The results of the simulation are presented and the implications are summarized.

Chapter 5 presents the experimental method including a description of the physical magnet prototype, the field measurement technique including radio frequency (RF) coil tuning, magnetic field scanning, pulse sequence and signal acquisition. The results of the experimental method are summarized and compared to the simulation results.

Chapter 6 provides conclusions, summary of contributions as well as potential areas for future work and improvements.

## 2 Background

The following section is a short background on the essential concepts of NMR necessary to understand the ideas presented in this thesis. Since the focus of our work relates to bulk time domain MR measurements, topics relating to image reconstruction such as slice selection and phase and frequency encoding were avoided. As the purpose of the background is to provide a brief overview of relevant material, the reader may find further clarification necessary. For a more detailed comprehensive overview of the material, the following NMR texts [70, 71] are suggested.

The background concludes with a description of the terminology and basic hardware components of a unilateral permanent magnet NMR system.

### 2.1 Magnetic Resonance

#### 2.1.1 Net Magnetization of Atomic Nuclei

Magnetic resonance is a phenomenon that depends on intrinsic properties of atomic particles. All particles display a quantum mechanical property known as spin angular momentum or simply “spin”  $I$ .  $I$  can be expressed as an integer, half integer or 0. Atomic nuclei with non-zero spins possess magnetic moments  $\mu$  that orient themselves in response to external magnetic fields and can be studied with MR methods [13]. Both

$\mu$  and  $I$  can be expressed as vector quantities as they possess both magnitude and direction [14].

In the presence of an external magnetic field, the randomly oriented magnetic moments will align with the field. The presence of the spin causes the precession of the magnetic moments around the field axis commonly defined as the  $z$ -axis, at a constant angle as illustrated in Figure 2.1

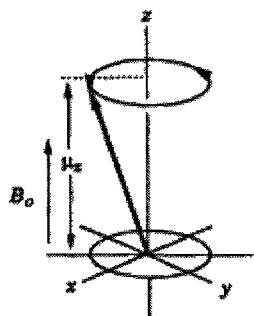


**Figure 2.1** [15] A vector representation of the precession of a magnetic moment around the  $z$ -axis of the  $B_0$  field is illustrated. The  $z$  component of the magnitude of the magnetic moment  $\mu$  is also indicated.

This can be understood as being analogous to the precession of a spinning top that is caused by the interaction of the top's angular momentum and the earth's gravitational field [14]. The coupling of nuclei of spin  $\frac{1}{2}$  (such as  $^1H$ ) with an external field – described as a *Zeeman Interaction* – results in only 2 possible orientations, parallel or anti-parallel to the magnetic field. In the presence of an external magnetic field, the parallel orientation is of lower energy and contains more spins than the anti-parallel orientation. The energy difference of the spin states – is given in [13] by

$$\Delta E_m = \frac{\gamma \hbar B_0}{2\pi} \quad 2.1$$

where  $\gamma$ ,  $h$  and  $B_0$  are the gyromagnetic ratio<sup>1</sup>, Planck's constant and external field respectively.

The precession frequency of the magnetization vector around the  $z$ -axis is defined as the Larmor Frequency or

$$\omega_0 = \gamma B_0 \quad 2.2$$

Energy absorption in the spin system occurs when the nuclei are irradiated with energy at the Larmor Frequency. This is typically accomplished through applying a short burst of radio-frequency (RF) energy – where the amplitude of the associated oscillating magnetic field is defined as  $B_1$  - perpendicular to the  $z$ -axis and the  $B_0$  field [16]. When RF energy at resonance is absorbed, a spin from the higher energy state is stimulated to descend to the lower energy state. Likewise low energy spins are excited towards a high energy state. A net absorption of energy occurs since more spins are found at a low energy state.

[14]

The number of protons in each energy level can be calculated through the *Boltzmann Distribution Function* which is given by [15] as

$$\frac{N_\beta}{N_\alpha} = \exp\left(\frac{-\Delta E}{kt}\right) \quad 2.3$$

where  $N_\alpha$  is the spin population at the lower energy state,  $N_\beta$  is the population at the higher energy state,  $k$  is the Boltzmann constant ( $1.3806503 [m^2 kg s^{-2} K^{-1}]$ ) and  $t$  is temperature [K].

---

<sup>1</sup> In this thesis the discussion is limited to the gyromagnetic ratio of  $^1H$  that is  $\frac{\gamma}{2\pi} = 42.58 \text{ MHz/T}$ .

Due to the greater number of parallel spins, addition of the magnetization vectors will result in a net magnetization vector  $M_0$  of constant magnitude oriented parallel to the  $B_0$  field.

The net magnetization vector  $M_0$  can be described by the Bloch equation given by

$$\frac{d\vec{M}}{dt} = \gamma \vec{M} \times \vec{B} \quad 2.4$$

that states that the rate of change of  $\vec{M}$  with respect to time is equal to torque on  $\vec{M}$  due to the magnetic field  $\vec{B}$  scaled by  $\gamma$ .

If  $B_{1xy}$  - an RF field oriented in the  $xy$  plane - is applied to the  $M_0$  net magnetization vector, the angle of precession will increase, resulting in the rotation of  $M_0$  towards the transverse  $xy$  plane by a given angle  $\alpha$ . The  $x$ ,  $y$  and  $z$  components of  $M_0$  can be described to rotate around the  $z$ -axis by

$$M_x = M_0 \sin\alpha \sin(\omega_0 t + \vartheta) \quad 2.5$$

$$M_y = M_0 \sin\alpha \cos(\omega_0 t + \vartheta) \quad 2.6$$

$$M_z = M_0 \cos\alpha \quad 2.7$$

where  $\vartheta$  is the angle of rotation with respect to the  $z$ -axis induced by  $B_{1xy}$ .

The  $M_0$  vector can be described in stationary or rotating (at precession frequency) frame of reference, although a rotating frame of reference is preferred due to the stationary vector representation.

### 2.1.2 Free Induction Decay

After application of an  $90^\circ$  RF pulse, defined as being of sufficient power or duration to tip  $M_0$  completely into the transverse  $x$ - $y$  plane (see Fig. 2.1), the nuclei will begin to reorient and align with the  $B_0$  field. If a receiver coil is placed perpendicular to the  $M_0$   $x$ - $y$  plane, the transverse component of magnetization  $M_{xy}$  (equation 2.5 and 2.6) will induce a voltage around the coil loop. The detected signal is called the *Free Induction Decay* or FID. The amplitude of the FID voltage is proportional to the magnitude of the  $M_0$  vector prior to the application of the RF pulse. The decay of the function provides information on the rate that coherence of the  $M_0$  spin is lost in a process described as *relaxation*. [17] The various forms of relaxation – as described in the next sections – provide the fundamental information required for techniques such as 1D time domain MR measurements and 2D contrast image reconstruction.

### 2.1.3 $T_1$ Relaxation

*Relaxation* is a time dependent process characterized by a constant known as the *relaxation time*. One of the measurable relaxation times is known as  $T_1$ .  $T_1$  or the *longitudinal relaxation time* is a time constant that characterizes the rate at which nuclei spins return energy to the system “lattice” and the  $M_0$  vector returns to equilibrium with the external field.  $T_1$  relaxation occurs due to energy interaction and exchange between neighboring spins. The return of the  $M_0$  magnetization vector to orientation with the  $B_0$  field along the z-axis is an exponential process governed by the expression

$$M_0(\tau) = M_0(1 - e^{-\frac{\tau}{T_1}}) \quad 2.8$$

where  $\tau$  is time elapsed since the cessation of the RF pulse [18]. After one  $T_1$  time constant, approximately 63% of the magnetization will have returned to equilibrium, whereas at 3  $T_1$  periods, over 95% of  $M_0$  will be aligned with the external field [18].

### 2.1.4 $T_2$ and $T_2^*$ Relaxation

The  $T_2$  time constant - or the spin-spin relaxation time - measures the rate at which the  $x$  and  $y$  components of  $M_0$  lose coherence and rotate out of phase. This phenomena occurs due to inter- and intra- molecular interactions that result in different spin frequencies and ultimately in a loss of the  $M_{xy}$  transverse magnetization component. The decay of the  $M_{xy}$  component is given by:

$$M_{xy}(\tau) = M_{xy} e^{-\frac{\tau}{T_2}} \quad 2.9$$

where  $\tau$  is defined as time elapsed since the cessation of the RF pulse and  $M_{xy}$  is the transverse magnetization component immediately after the application of the 90 degree pulse [18]. The  $T_2$  time constant is defined as the point where  $M_{xy}$  has decayed to only 37% of its maximal value. The loss of coherence can be attributed to non uniformities in the external field. Major factors that contribute to field fluctuations are: main field inhomogeneities due to magnet imperfections and field interactions with other objects and sample induced inhomogeneities due to differences of magnetic susceptibilities within the sample material. [18]. The total transverse relaxation time may be described as a summation of the factors that contribute to field inhomogeneities or

$$\frac{1}{T_2^*} = \frac{1}{T_2} + \frac{1}{T_{2m}} + \frac{1}{T_{2ms}} \quad 2.10$$

where  $T_2$  is the dephasing time experienced due to random spin interactions and  $T_{2m}$  and  $T_{2ms}$  are the time constants that describe dephasing due to the main field inhomogeneities and differences in sample magnetic susceptibilities [18]. Although  $T_2$  phase loss is an irreversible process, spin dephasing due to both  $\frac{1}{T_{2m}}$  and  $\frac{1}{T_{2ms}}$  can be reversed using a  $180^\circ$  RF pulse as discussed in the next section.

### 2.1.5 Hahn Echo

The Hahn echo proposed by Hahn et al. [19] provided a way to refocus the spin system after an initial period of loss of coherence. After the application of a  $90^\circ$  degree pulse, the system was allowed to dephase for a time constant  $\tau$ . A  $180^\circ$  degree RF pulse was then transmitted at the sample to “flip” and allow the spins to refocus.

### 2.1.6 Carr-Purcell-Meiboom-Gill Pulse Sequence

Further development of the Hahn echo led to the Carr-Purcell-Meiboom-Gill (CPMG) [20-21] sequence which can be written as  $90_x - (\tau - 180_y - \tau)^n$ . After rotating the spin system into the  $xy$  plane by application of a  $90^\circ$  pulse along the  $x$  – axis direction the spins are allowed to dephase for a time constant  $\tau$ . A train of refocusing echoes can be generated by subsequent application of  $180^\circ$  pulses that “flip” the spins in transverse plane as shown in Figure 2.2.

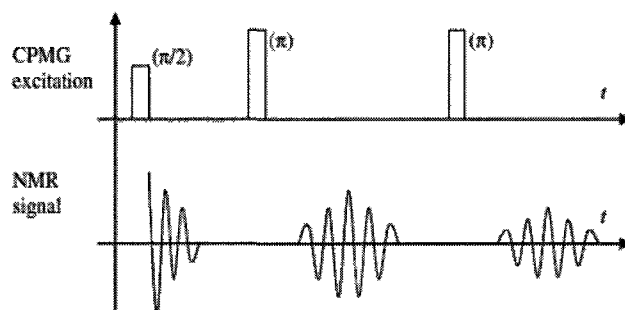


**Figure 2.2** [22] The CPMG pulse sequence consists of an initial  $90^\circ$  excitation pulse. After a period  $-\tau$  - the spins are refocused by a  $180^\circ$  pulse as shown by the " $\pi$  bar". After another  $\tau$  period an NMR signal echo can be noted. The  $180^\circ$  pulse is reapplied at  $\tau$  after the echo. The sequence of  $180^\circ$  pulses are repeated every  $2\tau$  to generate a train of echoes.

Although the Hahn and CPMG allows for spin refocusing, a decay of spin echoes is inevitable due to irreversible energy loss as a consequence of random intermolecular interactions. The time constant that describes this decay is defined as  $T_2$ .<sup>2</sup>

## 2.2 System Hardware Components of Unilateral NMR Sensors

The basic hardware components of classic and open NMR magnet systems share many similarities although important differences exist based on the unique requirements of each category.

The basic components required for MR experimentation are: 1. Hardware for generating a  $B_0$  field. 2. Hardware for generating the  $B_1$  RF field including a resonator and amplifier. 3. Signal detection hardware. 4. A control system required to precisely synchronize pulse sequence transmission and reception and 5. A data collection and processing system. The following section provides a brief discussion of the main system components.

### 2.2.1 $B_0$ Field

Conventional MRI scanners are designed to provide a strong homogeneous field, typically around 10 -50 ppm (parts per million) over a large volume – a 50 cm radius sphere for a 2 Tesla whole body system [23] and magnetic flux densities between 1.5 and

---

<sup>2</sup> The experimental section of this work (section 5) is based on signal amplitude measurements of a CPMG pulse sequence.

11.7 T [24]. Classical systems typically are based on helium cooled electromagnets to avoid the prohibitive energy cost associated with maintaining a powerful field with resistive coils [25]. The solenoidal coil closed bore design provides the highest homogeneity [8] and field strength [9] per volume although this is achieved at the cost of decreasing access to the scanning region.

The basic magnet homogeneity is improved further by inserting iron plates on the walls of the magnet bore and by the use of shim coils designed to compensate for magnetic field inhomogeneities in terms of spherical harmonics [23]. Gradient coils are inserted in the magnet bore housing [23] and are used to generate a linear variation in the  $B_0$  necessary for slice selection in imaging and other experiments.

One-sided permanent magnet designs are generally of much lower field strength – typically peaking at around .25 T – as well as reduced homogeneity with static field gradients as high as 20T/m [26, 42]. An extensive review by Blumich et al. [27] discusses different magnet array configurations designed to generate a remote homogeneous field. In practice however, inhomogeneities may be on the order of 1000-10000 ppm without further optimization of the field [27]. Field compensation by shim units using additional permanent magnets has been refined to include higher order derivatives of the field resulting in potential use for chemical-shift resolved NMR spectroscopy [28].

Although unilateral designs have been fitted with gradient coils capable of generating contrast images [29], significant limitations including small sensitive volume and long acquisition time have resulted in unilateral magnets being used primarily for bulk time domain measurements.

### 2.2.1 $B_1$ Field

RF coils are employed to generate a  $B_1$  field perpendicular to  $B_0$ . Common coil designs employed by superconducting magnets are the “saddle coil” and the “birdcage resonator” [23]. The saddle coil is an approximation of a cylinder with the coils oriented normal to the cylinder axis. A bird cage resonator is a ladder network comprised of inductive elements and distributed capacitors rolled into a cylinder form [30] that provides a sinusoidal current distribution that generates an internal homogeneous field.

In unilateral magnet designs, RF coils are distinguished by those that produce  $B_1$  fields perpendicular or parallel to the surface of the coil [27]. Selection of the appropriate coil depends on the orientation of  $B_0$ . When  $B_0$  is oriented perpendicular to the magnet surface a figure 8 coil with opposed current loops is generally used [27]. For an external field parallel to the magnet array surface a simple surface coil may be mounted on the magnets to provide a perpendicular  $B_1$  field.

RF coils can be categorized as *transmit* coils (Tx), *receive* coils (Rx) and *transmit/receive* coils (TxRx) [31]. Rx-only RF coils are generally found in MR systems that have a global body coil, whereas other MR applications such as ultra-high field and open configuration low field use TxRx coils [31].

The model and prototype design presented in this thesis (see 4.1 and 5.1) employs a TxRx surface coil mounted on the center of the magnet array.

RF coil loops can be tuned and matched by adjusting the capacitance of resonant circuits attached to the coil (see 5.4.2).

### **2.2.2 Signal Generation and Processing**

The hardware used in MR signal generation and processing including RF pulse generation, excitation, detection, amplification, filtering, A/D conversion and data display are similar in conventional and unilateral NMR magnets.

A control system drives a RF synthesizer to generate precisely timed pulses with high frequency stability. The pulse is then amplified by a high power RF amplifier and transmitted to the RF coil.

In RxTx systems, the weak signal from the coil is received and passed to a pre-amplifier. The NMR signal is filtered, amplified, demodulated in quadrature by multiplication with 2 sinusoids at the Larmor frequency  $90^\circ$  out of phase and digitally sampled by an A/D converter, before being stored on a computer with real and imaginary components corresponding to in-phase and quadrature signals respectively.

### **3 Literature Review**

In order to provide a historical context for the ideas and unique contributions presented in this thesis, the following section is devoted to a review of some of the major works in open geometry NMR magnet design. The focus of the discussion is an analysis of the advantages and disadvantages of each design especially in regards to SNR performance.

#### **3.1 Analysis of Open Geometry Mobile NMR Magnet Designs**

The first open NMR probes were developed in response to the oil exploration industry's need for a mobile device that could be used to study fluid properties in pores of rock formations. The resulting design was called the "inside out NMR" where instead of inserting the object to be sampled inside the device, the NMR probe was placed inside or alongside the sample under study [4].

For 30 years, the earth's magnetic field was used as the polarizing field  $B_0$  to examine rock strata in bore holes with limited success. Early designs included the Nuclear Magnetic Log developed by Gamson and Brown in 1960 [32]. Among the drawbacks of the early primitive devices was the poor sensitivity of the NMR signals due to the extremely weak polarizing field [4].

### 3.1.1 Homogeneous Field Designs

The low sensitivity of NMR signals generated from the weak magnetic field of the earth led to attempts to develop devices capable of generating an external strong homogeneous  $B_0$  field. Early efforts in the production of open NMR sensors focused on the development of devices capable of generating a region of local homogeneity or “sweet spot”. A sweet spot has been defined by Juan Perlo (2011) as “*a point in space where all first-order derivatives of the magnetic field magnitude are zero while the field strength is different than zero*”[33]. Improvements in field homogeneity allowed a greater sensitive volume, longer lasting NMR signals and consequently improvements in SNR. The disadvantages of these designs includes a loss in field homogeneity due to field cancelling effects and in most cases the need for complicated RF coil design due to the orthogonal orientation of the external  $B_0$  field instead of simpler more sensitive surface coils [34].

#### 3.1.1.1 Jackson Geometry

The first prototype that employed the use of permanent magnets to create an external  $B_0$  field was developed in 1980 by Richard Cooper and Jasper A. Jackson [35]. Cooper and Jackson describe the basic principle underlying the methods of remote field generation as “*If two equal field sources are arranged axially so their fields oppose in the region between them, then there exists a region near the plane perpendicular to the*

axis midway between the sources where  $H_r$ , the radial component of the field, goes to a maximum. Near the maximum, the field is homogeneous to within any chosen degree over prescribed regions.” As shown in Fig. 3.1, the Jackson geometry can be described as consisting of two axially aligned cylinder magnets facing each other with the same poles. The homogenous region is generated at the intersection of the opposing field lines which creates a sensitive volume “toroidal ring” in 3D space.

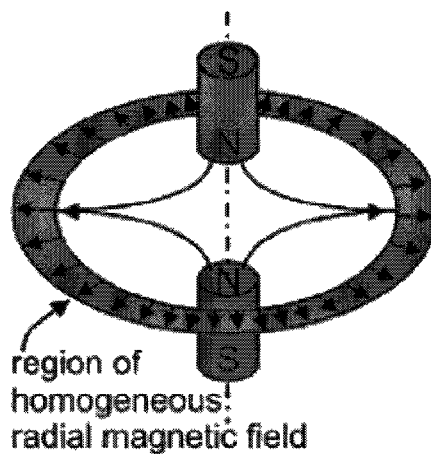


**Figure 3.1** [27] The “Jackson Geometry” generates a homogeneous toroidal field region through employing two opposed cylinder magnets at a fixed distance from a radial axis/plane.

Although the Jackson Geometry provided very good volume selection, the consequence of exciting a very small sensitive volume also led to a very low SNR. In an attempt to increase the sensitivity of the Jackson device, Clow, Percival and Walters (1986) [36] filled the RF coil with ferrite, changing the  $B_0$  field configuration and improving the sensitivity of the RF probe. Despite these improvements significant limitations remained, including the need for a nonmetallic housing for the probe as well as a relatively restricted sensed region diameter.

### 3.1.1.2 Schlumberger and Numar Designs

After the advent of the Jackson geometry, oil companies Numar (purchased by Haliburton in 1997) and Schlumberger independently developed 2 different open NMR sensors based on different magnet concepts [32].

The Numar MRIL (Magnetic Resonance Imaging Logging) tool, developed in 1991 for commercial oil well logging, used a long cylindrical magnet to generate a transverse magnetic field parallel to the borehole formation [37]. The RF coil is wound around the magnet and generates a  $B_1$  field perpendicular to  $B_0$ . Although a static field with a significant gradient is produced, the SNR is improved by increasing the overall field strength over the sensitive volume regions [32]. Since the  $B_0$  static field decays in strength as  $1/r^2$ , rings of different radius can be selected by choosing excitation frequencies matching resonance conditions, resulting in a number of sensitive volume “shells” (Fig. 3.2).

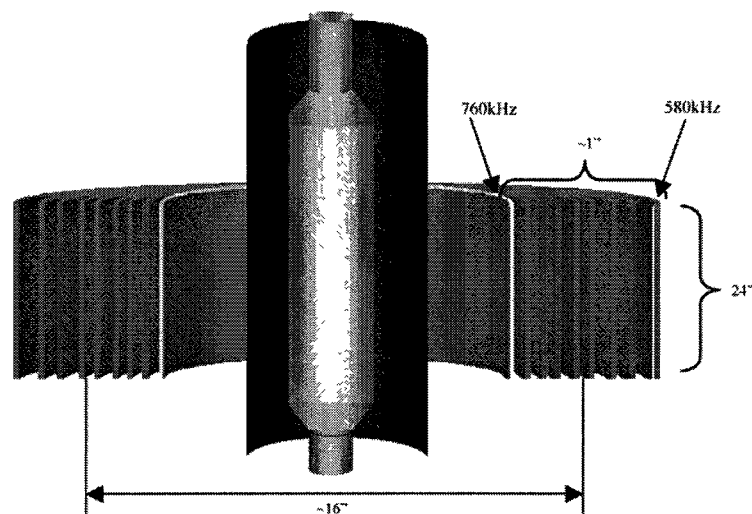


**Figure 3.2 [38]** Concentric “shells” of sensitive volumes generated by choosing excitation frequencies to spatially select slices of variable field strength.

Although the Numar MRIL significantly increased the sensitive volume and SNR by employing a permanent magnetic gradient [39], the specific design geometry and sensitive volume shells precluded its usage in other applications. In addition, the instrumentation housing had to be constructed out of nonmetallic materials to avoid interference between the RF coil and borehole formation.

In 1992 Kleinberg et al. [40] introduced a novel oil well logging NMR apparatus that formed the basis of the Schlumberger PNMT (Pulse Nuclear Magnetism Tool). The device utilized the Jackson Geometry concept of repulsive fields generating homogeneous regions [38]. Figure 3.3 demonstrates the magnet design and concept. 2 large bar magnets magnetized transverse to the borehole generate a homogeneous region called a “sweet spot” indicated in the box area enclosed by dashed lines. A 3<sup>rd</sup> smaller magnet is used to increase field strength without cancelling the sweet spot. The RF coil – labeled in Fig. 3.3 as “antenna” - is positioned between the exterior bar magnets.

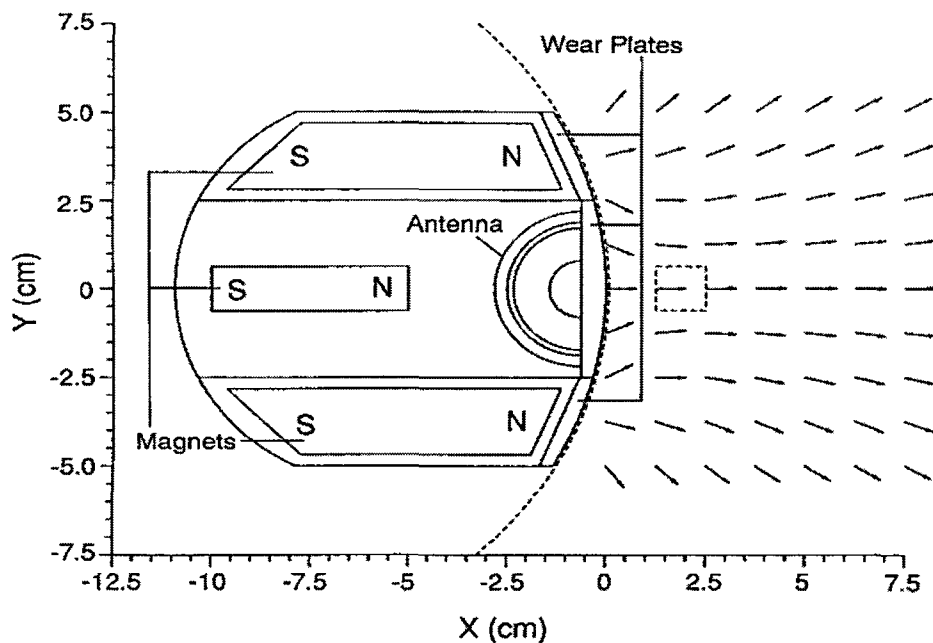


**Figure 3.3 [38]** The general scheme of the Schlumberger PNMT device is shown. The bar magnets generate homogeneous strong field to polarize samples in sensitive volume region. The rf coil - or antenna - transmits a perpendicular  $B_1$  field as well as receives NMR signals from the samples.

Although the Schlumberger device could be constructed with metal housing and utilized in a borehole of any diameter, serious limitations that remained included generation of a small sensitive volume resulting in a low SNR, as well as inaccurate measurements of borehole fluids [39].

Oil well logging devices marked the beginning of open MR designs; however these probes were unsuitable for general use due to unique constraints – long and narrow designs – necessary due to borehole geometry. In addition the length of these probes allowed a signal averaging over a large volume, resulting in a unique SNR advantage of these devices.

### **3.1.1.3 Unilateral NMR Permanent Magnet Designs**

As techniques used in oil well logging NMR improved, researchers began to realize the potentially vast number of applications for open geometry sensors. Early interest spanned diverse fields such as moisture detection in industrial materials [41] and soil [42], fat detection in food [42], and nondestructive testing of materials [43]. In addition applications in chemical spectroscopy [44] and medical diagnostics [29] have been developed. Early instruments were typically large and unwieldy and generally employed electromagnets operating at low frequencies [32]. It was not until the development of mobile unilateral permanent magnet NMR designs that the true potential and flexibility of these devices began to be realized.

Chang et al. (2006) [10] presents a single sided magnet based on the Halbach concept. The design consists of 8 radial magnetized cylindrical NdFeB magnets set into a

machined polyoxymethylene plastic steel holder. Each magnet is rotated  $90^{\circ}$  relative to its neighbour, generating a highly homogeneous strong field in its center and a moderately homogeneous region near the top of the magnet. This design generates a strong planar homogeneous field - measured at the center of the top of the magnet array at 0.2643 T - good for 1 dimensional profiling experiments and nondestructive evaluations of samples of large size; however a strong magnetic gradient can be detected above the surface of the magnet. Significant disadvantages of the devices may be attributed to a small sensitive volume and field inhomogeneities that negatively impact SNR. In addition, complex design may present a barrier to wide spread adoption of the device.

Another design by Chang et al. (2010) [45] describes a single – sided NMR apparatus consisting of a single disc shaped permanent magnet magnetized in the radial (horizontal) direction with a planar RF surface coil positioned above the magnet. A field strength of .279 T was found at the center of the upper surface of the magnet with the strongest field gradient of 10.27 T/m measured at 0.5mm < y < 1.5 mm vertically above the magnet. From 0 to .5 mm however, the symmetry of the stray field approximates a homogeneous region parallel to the magnetization direction. The simple design avoids the problems encountered in multiple magnet designs, such as differences in magnetic remanence, complex shim magnet designs, safety issues and complex manufacturing processes. In addition, the orientation of the field allows the use of a simple loop coil, increasing the apparatus' sensitivity. Challenges encountered with this design include low field strength - small sensitive volume due to field curvature at the magnet ends with a resultant loss of SNR. In addition, the simplicity of the design precludes any obvious way to control the field profile and homogeneity.

Other homogeneous field designs include the HALO (high access low oersted) system described by Routley and Carleton (2004) [7]. The device consists of 2 rings – each containing 16 NdFeB permanent magnets - separated by an air gap, with a combined field strength measured above the central upper surface of approximately 0.5 T. The external field profile can be controlled through adjusting the air gap distance. At an optimal spacing, a homogeneous central region is produced. Although the device is lightweight and portable, complicated design and low SNR present obvious disadvantages.

The barrel magnet is a geometry commonly used to generate homogeneous fields. Perlo [33] explains that two concentric bar magnets with different diameters and opposite polarization can cancel each other's field flux resulting in a sweet spot location where the gradient is 0. This effect can be duplicated by drilling a hole in the bar center allowing the positive polarization of the magnet and the negative polarization of the hole to cancel the field gradient in a region external to the magnet.

An adaptation of the barrel magnet geometry was used by Manz et al. (2006) [12] to build the NMR – MOLE (Mobile Lateral Explorer) - a device capable of generating a remote homogeneous field. The magnet array is based on a set of discrete cylindrical bar magnets spaced at set intervals on a circle, tilted towards a central bar magnet. Adjusting the angle and the size of the central magnet allows control over the position, strength and size of the homogeneous region. The field homogeneity allows characterization of  $T_2$  of liquids, avoiding the signal decay experienced in strong gradient fields due to diffusion effects. The low field strength – around 80 mT in the homogeneous region - as well as the complicated design, presents significant disadvantages.

A design presented by Perlo et al. (2006) [46] includes a main system consisting of 2 magnet blocks with opposite polarization set in an iron yoke separated by a central gap. The field homogeneity can be controlled through field cancellation effects by a shimming unit that produces a field with an opposite sign and gradient. The orientation of the field allows the usage of a simple surface coil, thus increasing the sensitivity and the SNR of the measurements. Marble et al. (2007) [47] described the disadvantages inherent in this configuration being due to size of the array necessary to allow the field to curl towards a horizontal (sweet spot) orientation, as well as a severe penalty in field strength and sensitive volume caused by zeroing the second spatial derivative of the field. Instead Marble et al. proposed a new magnet configuration based on adding a shim unit to a design described by Pulyer and Patz (1996) [48] where two axially magnetized and oriented magnets generate a sweet spot in the region above them (Figure 3.4). The advantages of such a design include, a safe low energy configuration, a compact design and a large homogeneous region as well as increased sensitivity due to a simple surface coil loop. The work in this thesis as described in section 4 and 5 is based on this design.

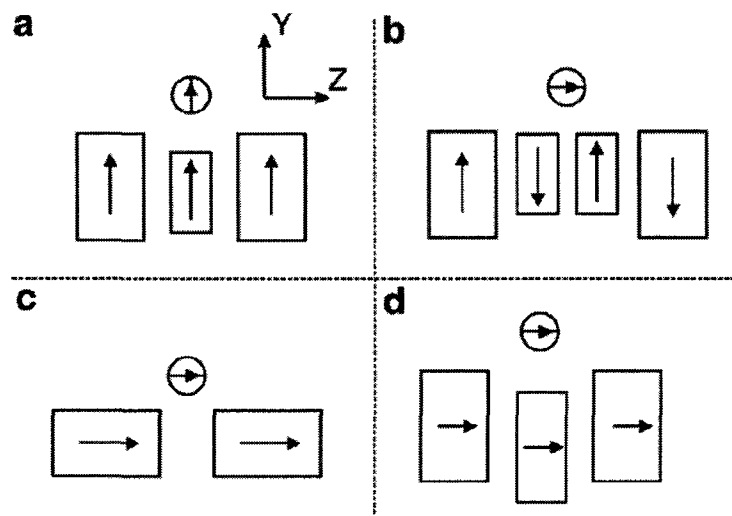


**Figure 3.4 [55]** (a)-(c) Different magnet configurations used to generate remote homogeneous fields. The arrows indicate the magnetization direction, the rectangles denote permanent magnets and the circles show the “sweet spots”. The design of (a) is used by Kleinberg et al [38]. (b) is a classical “u” geometry with shim units described by Perlo et al. [46]. (c) is the configuration used by Pulyer and Patz [48] and (d) is the novel configuration proposed by Marble et al. [47].

### 3.1.2 Inhomogeneous Field Designs

A second class of mobile NMR magnets has focused on creating strong static fields at the expense of homogeneity. Although magnetic field inhomogeneity is considered disadvantageous on several accounts including complications using conventional pulse sequences due to resonance offsets [49], and a loss of detection sensitivity due to a decreased sensitive volume [50], in other situations field inhomogeneities may prove beneficial such as measuring diffusion coefficients or high resolution sample profiling [11]. In addition, the static field strength of inhomogeneous designs can be greatly increased to compensate for much (or all – see 3.4) of the

sensitivity lost due to a reduced sensitive volume. Other advantages include simpler designs, reduced weight and cheaper manufacturing costs.

### 3.1.2.1 NMR-MOUSE

Development of portable NMR devices remained slow for a number of decades due to conflicting requirements of large magnets required for generation of strong fields vs. relatively lightweight materials required for device portability. The development of new magnetic alloys such as NdFeb and SmCo in the 1980's led to progress in mobile NMR design [51], but the first truly portable design – known as the NMR MOUSE (MOBILE Universal Surface Explorer) - was only developed in 1995 [52]. The NMR MOUSE was one of the first class of mobile one-sided magnets capable of measuring NMR signals from the side of an object, relaxing size limitations on samples [53]. The NMR MOUSE was based on a “u shaped” or horseshoe magnet design used to generate a strong stray magnetic field. The basic principle is the utilization of 2 magnet blocks with the opposite polarization to generate a static field parallel to the sensor surface [33].

Although the NMR-MOUSE generated a grossly inhomogeneous field with magnet field gradients up to 20 T/m [54], thus reducing the size of the sensitive volume, designers compensated for the reduced NMR signal sensitivity by increasing field strength.

The basic design of the NMR-MOUSE as demonstrated in Figure 3.5 consists of two anti-parallel permanent magnets that generate an inhomogeneous  $B_0$  static field. An RF coil situated in the gap between the magnets produces a  $B_1$  f field. The sensitive

volume, where the field lines intersect orthogonally the field, is indicated in the shaded area.

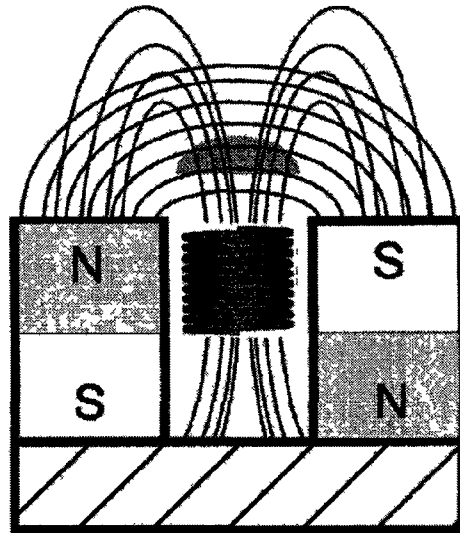


**Figure 3.5:** The basic design of the NMR-MOUSE [55] consists of two permanent magnets with anti-parallel magnetization and a RF coil. The NMR signal is generated in the sensitive volume shown by the shady area.

The compact design of the NMR-MOUSE, the high field strength (up to 0.5 Tesla above the surface of the magnet [32]) and the adjustable gradient are some of the factors that have contributed to the success of the device. The NMR-MOUSE has been used in a wide range of fields including non-destructive testing of polymer products [56], food analysis [57], as well as testing of materials of cultural and historical value [58].

After the possibility of extracting NMR measurements from inhomogeneous fields had been validated, a simpler version of the NMR-MOUSE consisting of a single bar magnet was described by Blumich et al. (2002) [59]. The price paid for the simple

design included a loss of some sensitivity due to perpendicular orientation of the  $B_0$  field relative to the magnet surface, necessitating the need for a complex coil design.

### 3.2 Field Homogeneity vs. Field Strength

A review of two basic philosophies of unilateral NMR magnet design has been presented. Since the signal-noise-ratio of MR measurements is proportionate to field strength and homogeneity according to  $\text{SNR} \propto B_0^2 \propto \frac{1}{\Delta B_0}$  [11] where  $\Delta B_0$  is the magnetic field inhomogeneity, increasing either factor is an obvious strategy to improve device performance.

One approach as expressed by Jackson [35], Kleinberg [38] and Perlo [33] was to increase signal sensitivity by designing a device capable of generating a remote homogeneous region or a “sweet spot”. The other approach taken by Eidmann et al. [52] in the design of the NMR-MOUSE, was to compensate for a reduced sensitive volume due to field inhomogeneities by increasing field strength.

Since field strength and field homogeneity are “antagonistic parameters”, i.e. improving one comes at the cost of reducing the other [60], an important research goal is to investigate which parameter plays a greater role in increasing the signal to noise ratio.

Although in some cases it may be desirable to have a device with a weak highly homogeneous field or a strong grossly inhomogeneous field, in most situations finding the optimal balance between field strength and homogeneity is the best way to increase the device performance.

The question we can ask is thus twofold; 1: does field strength or field homogeneity have a greater influence on increasing SNR and 2: how can these parameters be optimized?

The implications of the results of this research may lead to the conclusion that either inhomogeneous field or homogeneous field devices provide optimal SNR performance, thus validating one of the 2 general approaches mentioned earlier. In addition, a general method of parameter optimization may prove useful for further unilateral NMR magnet design and research.

Although an expression has been derived by F. Casanova et al. (2011) [11] that relates the SNR of unilateral probes to the product of  $B_0^2$  and field homogeneity – a general analytical solution is difficult to calculate for a number of reasons. Determining SNR is dependent on precise knowledge of field homogeneity and field strength. In addition the particular SNR performance of each design is dependent on such factors as RF circuit bandwidth, signal response function and resistance and temperature of the coils [11]. Since many of these parameters differ for various magnet designs, an SNR comparison between different models was deemed impractical.

We decided to follow an empirical approach based on results derived from simulating a magnet design prototype. A 2D slice of a unilateral “sweet spot” magnet design (described in Chapter 4) with an adjustable central shim unit was modeled through MATLAB software. Lowering the unit weakens the field and increases homogeneity – thus representing a typical tradeoff of these parameters. Simulating a range of shim unit displacements, the maximum signal density (an approximation of the SNR see 4.2.4) was calculated. The optimal field strength and homogeneity was identified as the shim unit

configuration that generated the maximum signal density. Simulation results -although design specific – may still prove useful in indicating whether field strength or homogeneity play a greater role in maximizing SNR. In addition, the simulation approach may be applied without great difficulty to magnet designs of different geometries.

### **3.3 Conclusion**

A review of current and past unilateral magnet designs leads to the conclusion that the models may be categorized as homogeneous and inhomogeneous field devices. It is unknown however which of these parameters play a greater role in SNR optimization. An empirical approach based on simulation of a NMR magnet design allows computation of the shim unit configuration that generates the maximal SNR. These results show the magnet displacement that provides the optimal balance of field strength vs. homogeneity and prove that field homogeneity is the dominant factor in maximizing SNR (see 4.3). The simulation may also be extended to other design geometries.

## 4 Model Simulation

This chapter provides a description of our model simulation including: magnet design dimensions, parameters such as the  $B_0$  and  $B_1$  field, frequency bandwidth used, assumptions used in calculating signal sensitivity, as well as the overall flow of the algorithm. The simulation was implemented with MATLAB R2009a software. We conclude with analysis and discussion of the results.

### 4.1 Model Description

The model simulated in this thesis is based on the design presented by Marble et al. [47] consisting of 3 NdFeB bar magnets magnetized along the z-axis (Figure 4.1). The magnets have a uniform thickness of  $t = 50$  mm. The outer magnets have a width of  $w=30$  mm, while the inner magnet has a width of  $w= 20$  mm. The additional depth dimension,  $d = 100$  mm, of the 3D laboratory prototype used in the experimental section of the thesis (see Chapter 5), was ignored in our 2D model. The surface coil position is shown in Fig. 4.1 set above the center magnet.

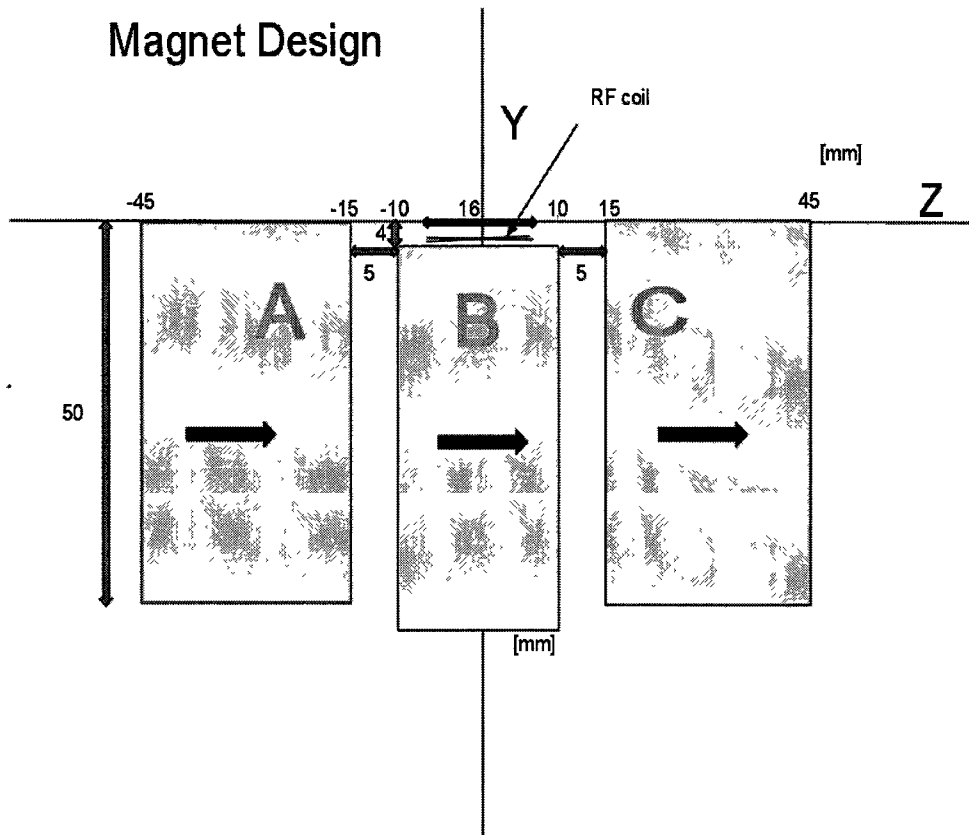


**Figure 4.1.** A 2D representation based on the Marble et al. design [47] is shown. The 3 bar magnets labeled A, B and C from left to right, are centered on the  $y$ -axis and are positioned below the  $z$ -axis. The magnetization direction is indicated by arrows parallel to the  $z$ -axis. The magnets have a uniform thickness (height in the diagram) of 50 mm and a width of 30 mm and 20 mm for the outer and central magnet/s respectively. The center magnet can be adjusted along the vertical  $y$ -axis. The magnets were uniformly spaced by 5 mm. A 16 diameter coil used in NMR measurements is shown above the center magnet.

## 4.2 Signal Optimization

This section provides a detailed explanation of the key components of the simulation. We develop an expression defined as  $S_{max}$  or maximum signal density that approximates SNR. A detailed analysis is provided of the methods used to calculate the individual parameters of  $S_{max}$  including  $B_0$ ,  $B_1$ , center bandwidth frequency values and

bandwidth boundaries. Finally, the stages of the algorithm flow are summarized in flow chart form (4.2.7).

#### 4.2.1 Calculation of Maximum Signal Density

One of the major goals of this work is to develop a reasonably accurate yet simple method of simulating signal output for different magnet array configurations during a common pulse sequence such as CPMG.

Although an analytical expression for the SNR of an NMR experiment was initially derived by Abragam [61] and later by Hoult and Richards [62], their work was not considered to have included conditions typical of one-sided sensors such as highly inhomogeneous fields, off-resonance excitation and inhomogeneous RF fields.

Work by a number of authors [63,64] have dealt with formulating expressions that characterize the response of a spin system in an inhomogeneous magnetic field and its contribution to the measured NMR signal.

Hurlimann et al. [63] provides a general expression for the voltage induced in a coil from inhomogeneous fields as

$$V_{x,t}(t) = \frac{2\chi}{\mu_0} \int dr \Phi(r) B_0^2(r) \frac{\omega_1(r)}{I} F(\Delta\omega_0(r)) m_{x,y}(r, t) \quad 4.1$$

where  $\chi$  is the nuclear magnetic susceptibility,  $\mu_0$  is the permeability of free space,  $\Phi$  is the phase of the RF pulse and  $m_{x,y}(r, t)$  is the transverse magnetization at point  $r$  and time  $t$ .  $F(\Delta\omega_0)$  is the frequency response of the system and  $\frac{\omega_1(r)}{I}$  or the RF frequency at point  $r$  over current  $I$  is the coil efficiency at detecting magnetization at point  $r$ .

Another approach taken by Balibanu et al. [64] relies on computing the signal by analyzing the evolution of the spin system absorbing RF energy from a pulse sequence. The actual signal generated in a unit volume that can be detected at time  $t$  is given by

$$S_{x,y}(t) = 2\chi\gamma \int_V B_0^2(r)B_{1n}(r)C_{1,2}(r,t)f(\gamma B_0(r)) dV \quad 4.2$$

where  $C_{1,2}$  are coefficients of a density operator described by

$$\rho(t) \propto [C_1(t)I_x + C_2(t)I_y] \quad 4.3$$

where  $I_x$  and  $I_y$  are the  $x$  and  $y$  components of a density matrix that can be used to describe the evolution of the spin system under the action of a pulse sequence.

$f(\gamma B_0(r))$  is a function that describes the frequency distribution of a signal.

Some of the disadvantages of these approaches involve the relative complexity of computing parameters such as RF pulse phase, system frequency response, spatial distribution of transverse magnetization and density operator coefficients. Although Casanova et al. [11] provides an analytical solution for unilateral magnet SNR for a CPMG sequence, this equation was not utilized due to the complexity of determining components of the equation such as the coil efficiency, inductance of the coil and RF power.

In order to simplify signal optimization of our device, we use a parameter introduced by Balibanu et al. [64] defined as the *maximum signal density* or

$$S_{max}(r) = 2\chi\gamma B_0^2 B_{1n} \quad 4.4$$

where  $B_{1n}$  is defined as the components of the  $B_1$  field that are orthogonal to  $B_0$ .

If we can assume that the noise of our device is relatively constant for different magnet geometries, we can hypothesize that the magnet configuration that generates the highest maximum signal density also provides the highest SNR.

Due to field inhomogeneties,  $S_{max}$  can be computed over a large spectrum of frequencies. In order to account for the system spin dynamics - as discussed by Balibanu et al. [64] - in a simple way, we assume that only the part of the system within a bandwidth corresponding to a pulse width at FWHM (full width half maxima) of  $\pm 100$  KHz or  $5 \mu s$  gets excited. This bandwidth was chosen based on experimental results that show that  $90^\circ$  pulses required for generating a signal maximum were about  $5 \mu s$  in length (see 5.4.3 and 5.4.4). We can therefore add limits to eq. 4.4 and write

$$S_{max}(r) = \int_{BW2}^{BW1} 2\chi\gamma B_0^2 B_{1n} ds \quad 4.5$$

where  $BW1$  and  $BW2$  are the contours corresponding to the upper and lower cutoff bandwidth respectively and  $ds$  is an element of the area between the bandwidth limits.

By integrating  $B_0^2$  over this region only, we account for the inhomogeneity of the field.

According to eq. 4.4  $S_{max} \propto B_0^2$ , therefore increasing  $B_0$  will cause  $S_{max}$  to rise.

However as the field homogeneity decreases, the region where  $S_{max}$  is integrated is reduced as the bandwidth becomes narrower. These opposing trends lead to a tradeoff of field strength vs. homogeneity in calculating the maximum possible value for  $S_{max}$  in equation 4.5. Our goal is therefore to determine the optimal balance of field strength vs.

homogeneity that generates the most signal density for a given magnet array configuration.

#### 4.2.2 $B_0$ Field Simulation

An equation for a magnetic field due to a bar magnet has been derived by Marble et al. (2007) [47] by approximating a permanent magnet in 2D as a pair of sheets of current. The bar magnet is magnetized along the  $z$ -axis and positioned with its upper surface centered on the origin and its width and thickness are represented by  $w$  and  $t$  respectively (Figure 4.2).

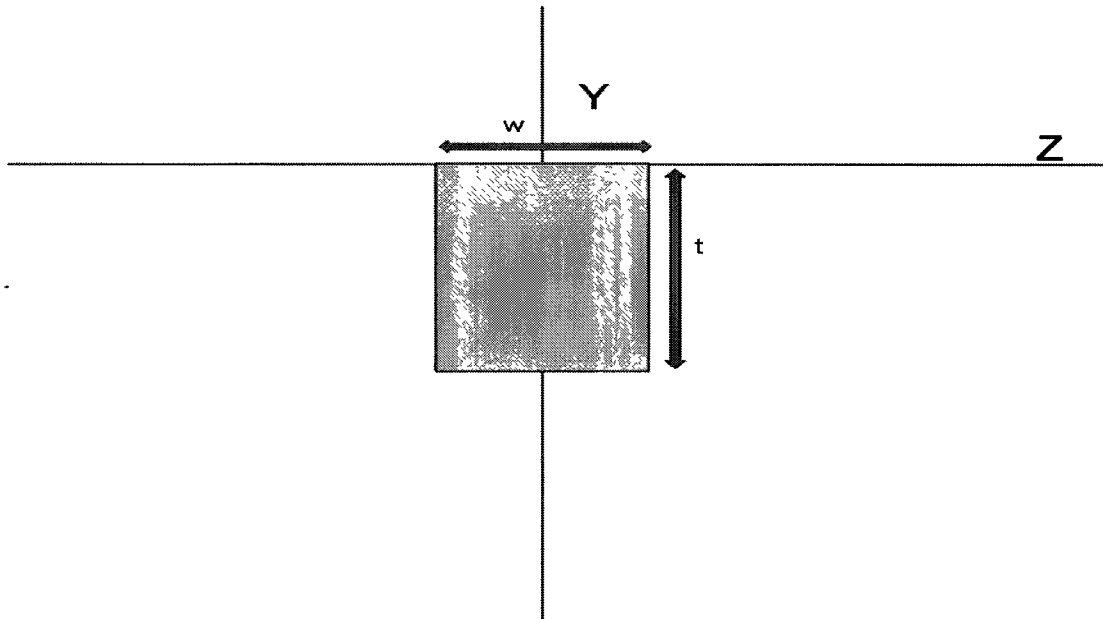


**Figure 4.2.** The upper surface of the magnet is centered under the origin of the  $y$  and  $z$  axis. Width and thickness of the magnet are defined by the parameters  $w$  and  $t$ .

If the depth of the magnet along an imaginary  $x$ -axis is envisioned as being infinite in two dimensions, the bar magnet can be represented by two sheets of current  $I$  along its upper

and lower surface (Figure 4.3). Using the right hand rule, it can be determined that the current flows out of the page along the magnet's upper surface and flows into the page at the lower surface. The current can be divided into infinitesimal line currents of width  $dz'$ . The magnetic field of each element can be calculated by using Amperes law for an infinitely long straight wire,

$$\vec{B}' = \frac{\mu_0 I}{2\pi r'} \hat{\theta}' \quad 4.6$$

where  $\mu_0$  is the permeability of free space ( $4\pi * 10^{-7} \frac{T*m}{A}$ ),  $I = Idz'$  is the current of every current line element,  $r'$  is the distance from the wire to an observation point and  $\hat{\theta}' = -\sin\theta' \hat{z}' + \cos\theta' \hat{y}'$  is the unit normal of the angle in polar coordinates.

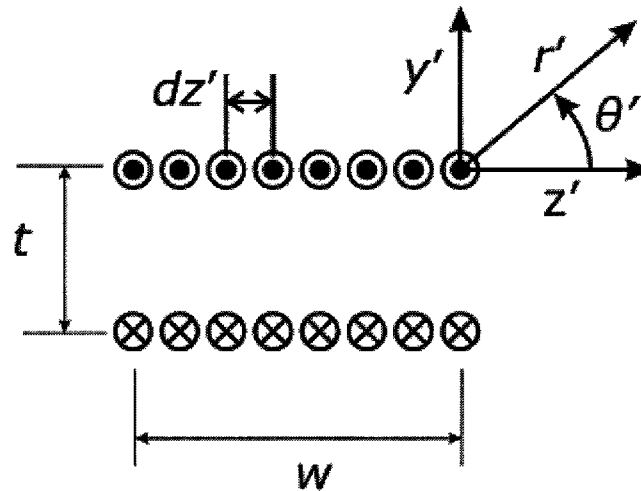


**Figure 4.3.** [47] The bar magnet can be represented by two sheets of current composed of infinitely deep line current elements of width  $dz'$ . The circles with black centers and circles with crossed centers represent current flow out of and into the page respectively.

After converting to Cartesian coordinates, the field due to the upper sheet of current can be written as

$$\vec{B}_{top}(z, y) = K \left[ - \int_{-w/2}^{w/2} \frac{y}{(z - z')^2 + y^2} dz' \hat{z} + \int_{-w/2}^{w/2} \frac{z - z'}{(z - z')^2 + y^2} dz' \hat{y} \right] \quad 4.7$$

where  $= \frac{\mu_0 I}{2\pi}$ . After integrating and using the relationship  $\vec{B}_{bottom} = -\vec{B}_{top}(z, y + t)$

, the total field of the bar magnet can be expressed as

$$\begin{aligned} \vec{B}(z, y) = K & \left[ - \tan^{-1} \left( \frac{z - w/2}{y} \right) + \tan^{-1} \left( \frac{z + w/2}{y} \right) + \tan^{-1} \left( y + \frac{z - w/2}{y + t} \right) + \right. \\ & \left. \tan^{-1} \left( \frac{z + w/2}{y + t} \right) \hat{z} \right] + \frac{K}{2} \left[ \log \left( \frac{y^2 + (z + w/2)^2}{y^2 + (z - w/2)^2} \right) \right. \\ & \left. - \log \left( \frac{(y + t)^2 + (z + w/2)^2}{(y + t)^2 + (z - w/2)^2} \right) \right] \hat{y} \end{aligned} \quad 4.8$$

A contour plot of  $|B_0|$  generated (using equation 4.8) by the simulation model (described in Figure. 4.1) is presented in Figure 4.4 A. Figure 4.4 B shows a zoomed in plot of the “sweet spot” shown as the largest open area between contour lines.

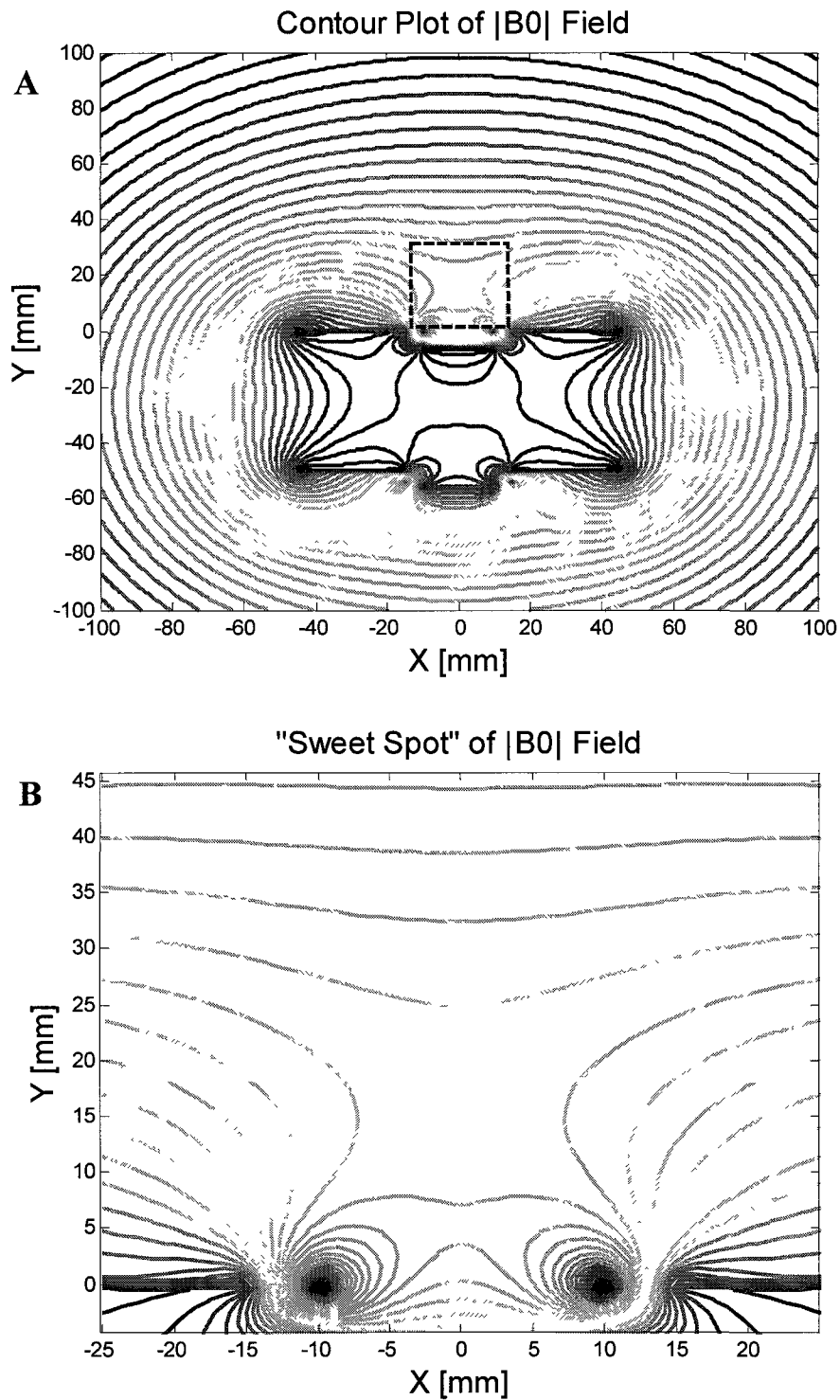


**Figure 4.4.** **A:** The contour map of the  $|B_0|$  field is shown for a central magnet offset of -6 mm. The map provides information on the spatial variations in field strength and homogeneity. A dashed box surrounds the homogeneous region otherwise known as a “sweet spot”. **B:** This zoomed in plot of **A**, shows a “sweet spot” or a homogeneous field region that can be identified by the relatively large gap between the field lines.

Since every point on a contour line represents the same field strength, variations of field homogeneity can be viewed as function of the distance between the lines. The larger the gap between contour lines, the greater the field homogeneity and vice versa.

In order to scale the simulation with our laboratory prototype (see 4.1 and 5.1), a scaling factor was introduced that converted the Larmor frequency corresponding to field strength to 4.55 MHz at 10 mm above the center of the upper surface of the central magnet at the center of the sweet spot for an offset of -4 mm.

#### 4.2.2 $B_1$ Field Simulation

The  $B_1$  field of a simple 16 mm diameter surface coil, set slightly above the central magnet, was simulated using equations 4.9 and 4.10 (reproduced from [65])

$$B_y = A \frac{1}{\pi\sqrt{Q}} \left[ E(k) \frac{1 - \alpha^2 - \beta^2}{Q - 4\alpha} + K(k) \right] \quad 4.9$$

and

$$B_r = A \frac{\gamma}{\pi\sqrt{Q}} \left[ E(k) \frac{1 + \alpha^2 + \beta^2}{Q - 4\alpha} - K(k) \right] \quad 4.10$$

where  $B_y$  is the magnetic field component aligned with the coil axis ( $y$ -axis in Fig. 4.1) and  $B_r$  is the magnetic field component in the radial direction of the coil ( $z$ -axis in Fig. 4.1).  $A$  – the magnetic field in the center of the coil – is defined as in [65]

$$A = \frac{i\mu_0}{2a} \quad 4.11$$

where  $\mu_0$  is the permeability of free space,  $i$  is the current in the wire in amperes and  $a$  is the coil radius.  $\alpha$  is defined as  $r/a$  where  $r$  is the radial distance from the axis of the current to an observable point,  $\beta$  is  $x/a$  where  $x$  is the distance on axis from the center of the current loop to the field measurement point and  $\gamma$  is equal to  $x/r$ .  $Q$  is defined as  $[(1 + \alpha)^2 + \beta^2]$  and  $k$  is equal to  $\sqrt{\frac{4\alpha}{Q}}$ .  $K(k)$  – the complete elliptic integral function of the first kind – is defined as [66]

$$K(k) = \int_0^{\frac{\pi}{2}} \sqrt{(1 - k^2 \sin^2 \theta)} d\theta \quad 4.12$$

and  $E(k)$  – the complete elliptic integral of the second kind – is defined as [66]

$$E(k) = \int_0^{\frac{\pi}{2}} (1 - k^2 \sin^2 \theta)^{\frac{1}{2}} d\theta \quad 4.13$$

Since it is  $B_{1n}$ , the orthogonal component of  $B_1$  that acts on  $B_0$ , the orientation of the RF coil field is of particular importance. Figure 4.5 A, B compares  $B_1$  and  $B_0$  normalized vector field direction. As shown in Figure 4.6, the sensitive volume of the sample is located at the region where orthogonal components of the  $B_0$  and  $B_1$  fields intersect.

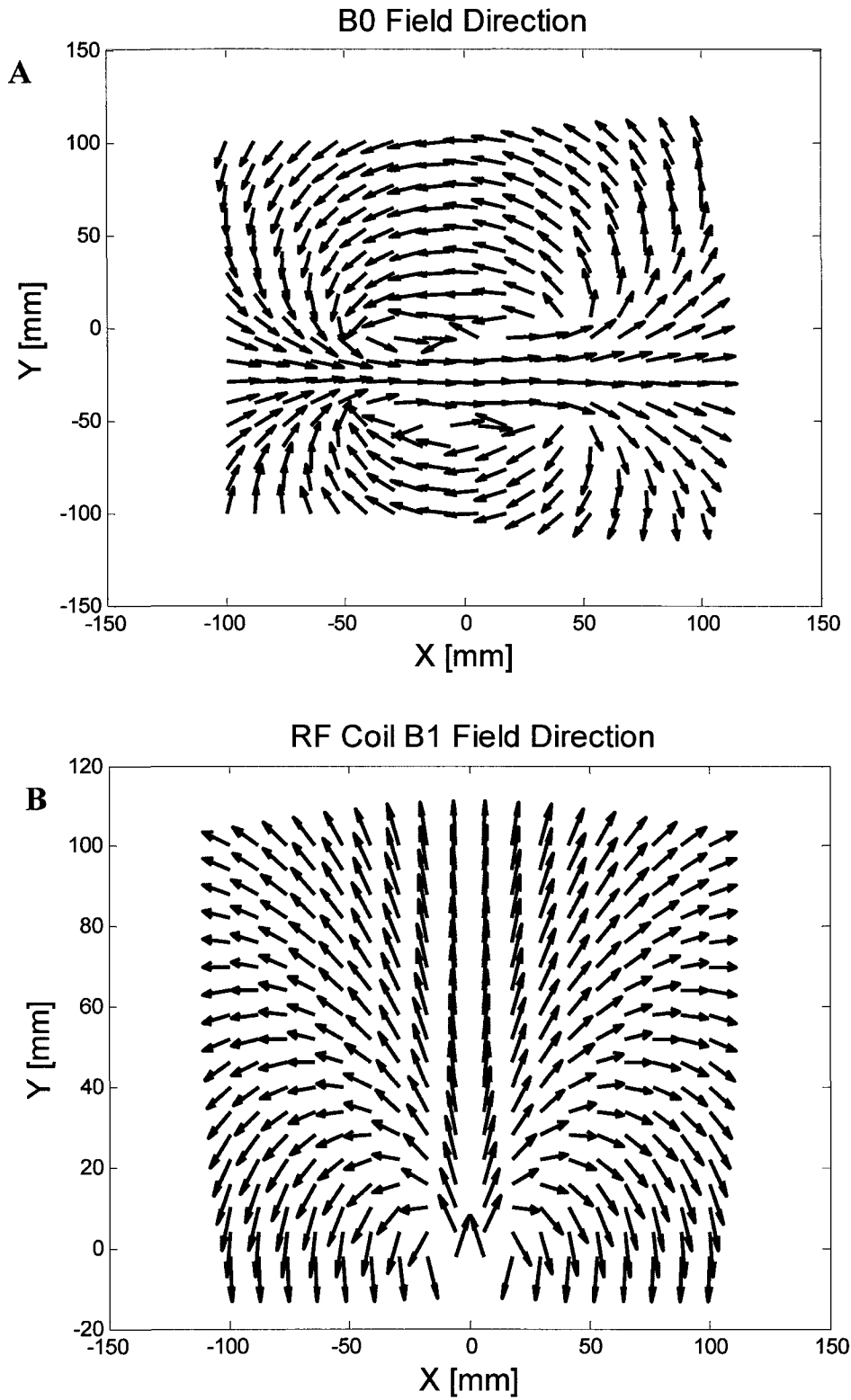


**Figure 4.5.** The direction of a normalized vector field is shown for **A:** the magnet array  $\mathbf{B}_0$  field and **B:** the RF coil loop  $\mathbf{B}_1$  field. The generation of  $\mathbf{B}_1$  field components orthogonal to the  $\mathbf{B}_0$  field ensures the possibility of simulating NMR signals.

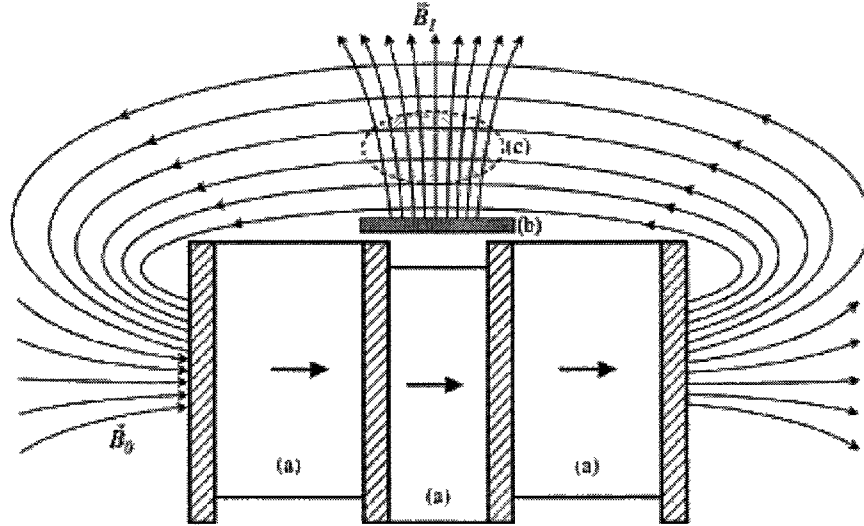


**Figure 4.6** [67]. The orientation of the  $B_0$  and  $B_1$  fields are shown. (a) shows the magnetization direction of the bar magnet array, (b) indicates the position of the RF coil (not to scale) and (c) shows the sensitive volume region where orthogonal components of the  $B_0$  and  $B_1$  fields intersect.

### 4.2.3 Calculation of $B_{1n}$

Assuming that the spin dynamics of a system are determined solely through the interaction of the  $B_1$  field on a sample in  $B_0$  and that  $|B_1(r, t)| \ll |B_0(r, t)|$  [63], we only have to consider the components of  $B_1$  perpendicular to  $B_0$  or the  $B_{1n}$  field which is given by equation 4.14 (reproduced from [63])

$$B_{1n} = \frac{1}{2} \left[ B_1(r) - B_0(r) \frac{B_1(r) \cdot B_0(r)}{B_0(r) \cdot B_0(r)} \right] \quad 4.14$$

Although the time dependent spin dynamics of the system are not calculated in this simulation (see 4.2.4), the same principle can be applied to a non dynamic interaction as long as the condition  $|\mathbf{B}_1(\mathbf{r})| \ll |\mathbf{B}_0(\mathbf{r})|$  is valid. Figure 4.7 shows the direction of the normalized  $\mathbf{B}_{1n}$  vector field. In practice however, signal attenuation occurs proportionate to the square of the distance from the coil, and for elements of  $\mathbf{B}_1$  that are not completely perpendicular with  $\mathbf{B}_0$ .

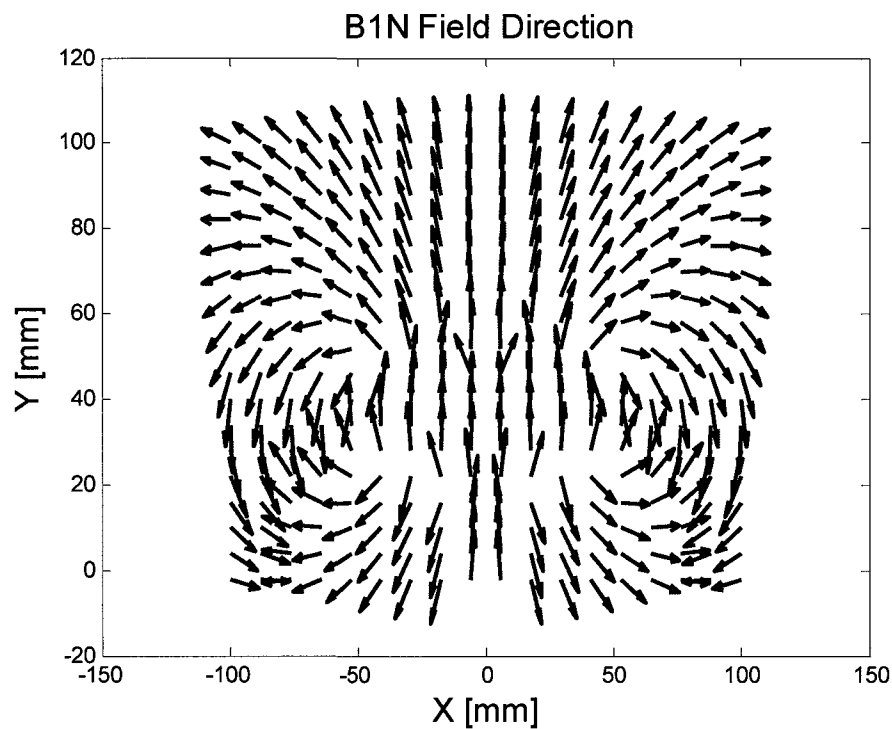
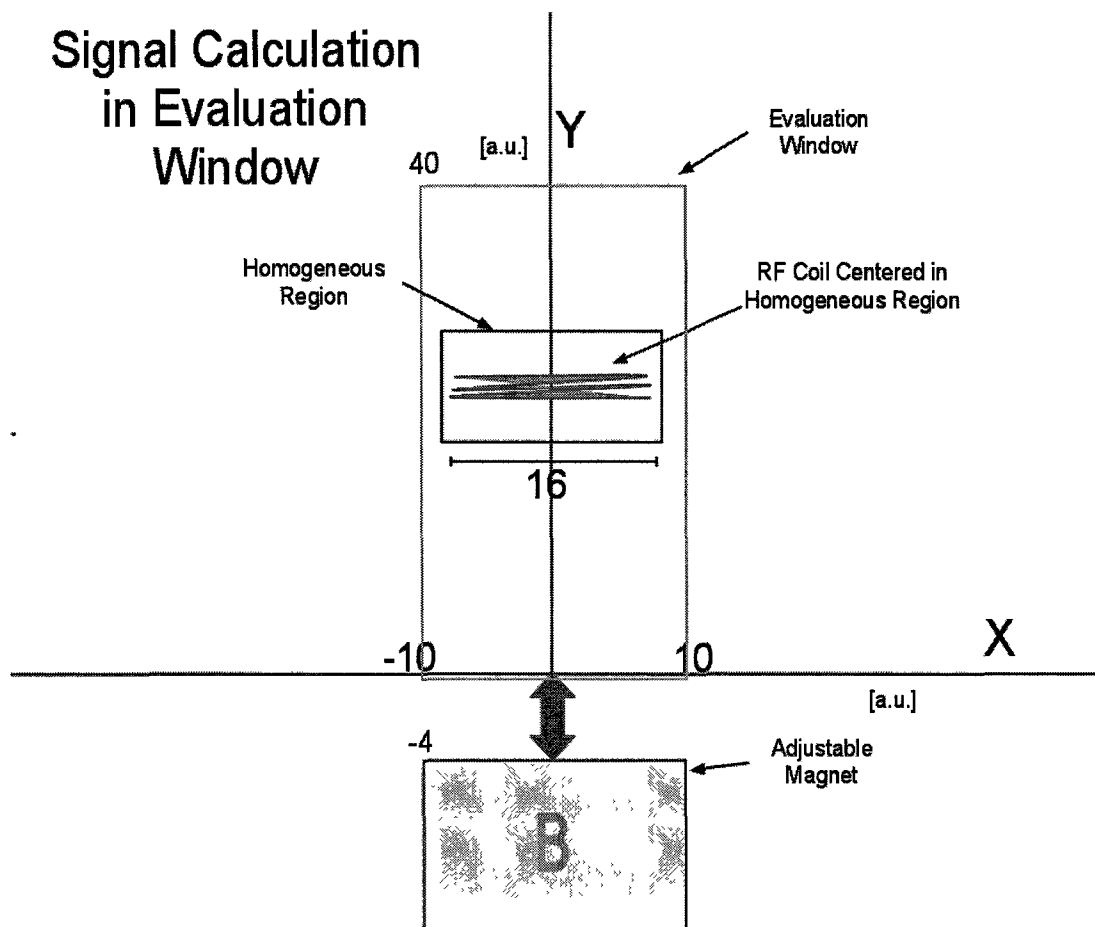


**Figure 4.7.** The direction of the normalized  $\mathbf{B}_{1n}$  vector field is shown. In practice, an effective signal is only generated in a region proportional to the diameter of the RF coil.

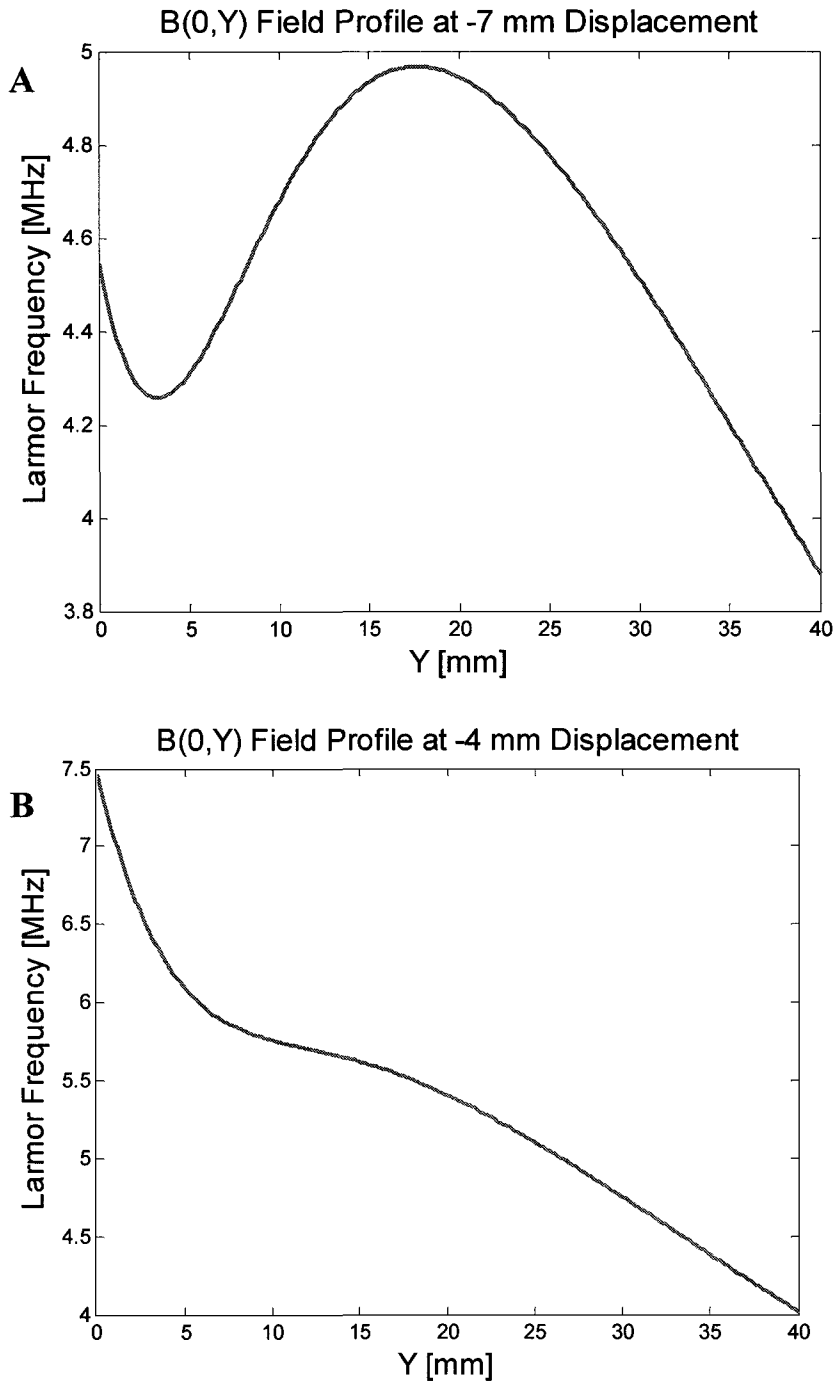
#### 4.2.5 Setting Evaluation Window Boundaries

One of the goals of the simulation was to develop a method of measuring the best signal. One of the first steps of this approach was to determine an optimal “evaluation

window” where signal density could be computed for different magnet displacements. We accomplished this by analyzing the changes of a 1D profile of a  $B_0$  field slice - extending vertically above the surface of the central magnet – for a range of displacements. Results of this analysis showed that to consistently integrate the signal over the entire “sweet spot” bandwidth, the evaluation region should be defined as a rectangular window of dimensions -10 to 10 mm along the z-axis and 0 to 40 mm along the y-axis centered above Magnet B. The field profile in this region was the most responsive to central magnet displacements and contained the highest stray field strength and/or homogeneity above the magnet array surface. In the event of displacements along the positive y-axis, the window was programmed to move just above the central magnet while maintaining its spatial dimensions. Figure 4.8 illustrates a diagram of the central adjustable magnet, the rf coil and the evaluation window where the signal was calculated. Figure 4.9 A, B illustrates some field profiles in the defined evaluation window for different magnet configurations.



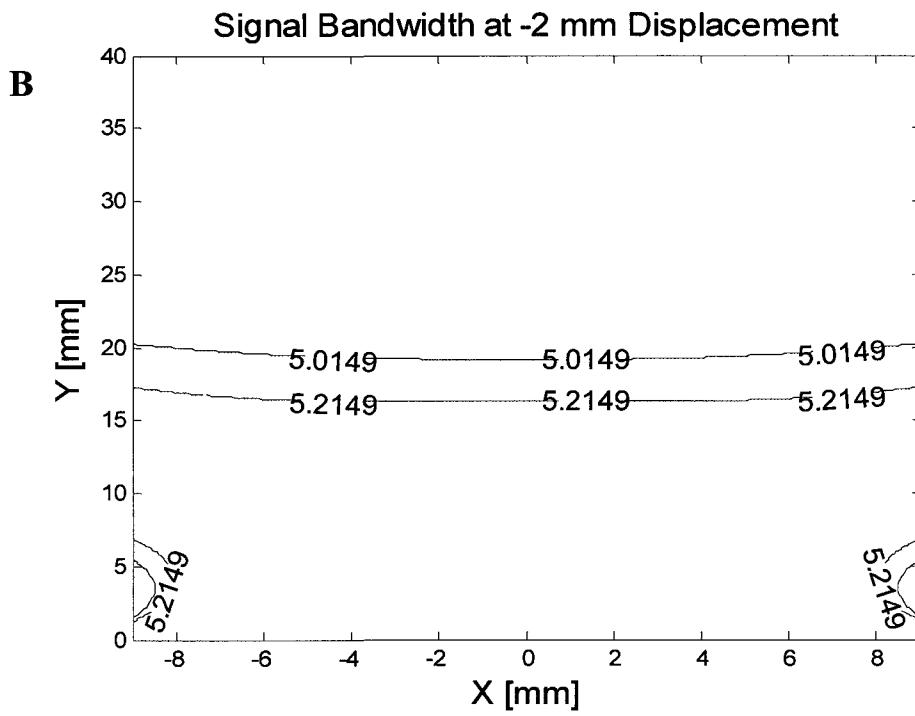
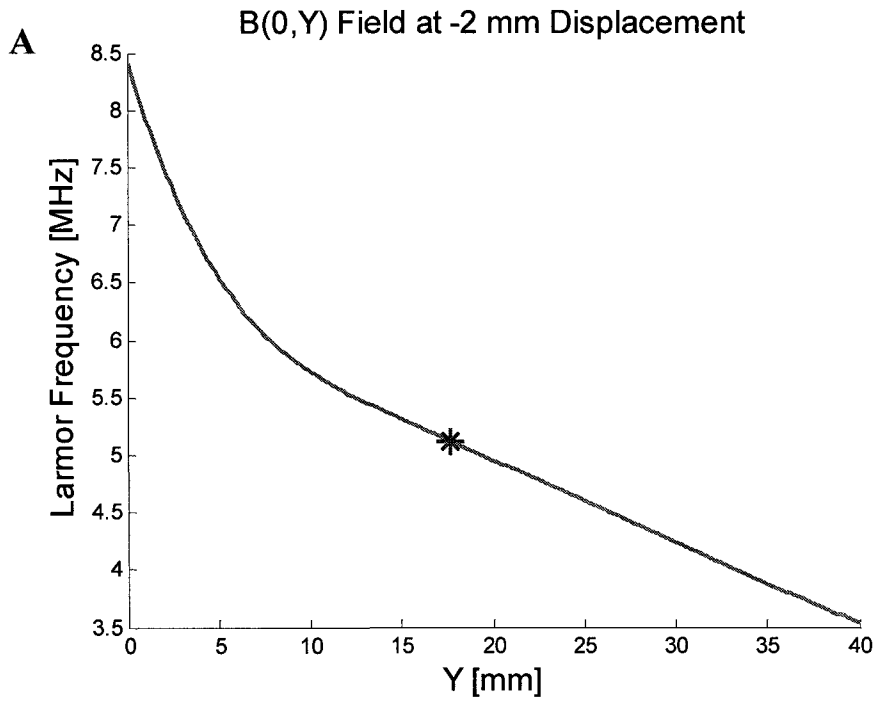
**Figure 4.8.** A schematic diagram is shown of the configuration used to calculate the NMR signal. The signal is integrated in the evaluation window 20 mm wide and 40 mm thick for a central magnet displacement of - in this case - 4 mm. The 16 mm coil is shown centered at the homogeneous region – defined as the field extrema or saddle points (see 4.2.6). Magnets A and B are not shown for clarity.



**Figure 4.9.** 1D profiles of a central slice of the  $B_0$  field. **A:** At -4 mm displacement below the z-axis no field extrema can be noted but the field strength corresponding to area under the graph is larger than **B**. **B:** At -7 mm local maximum can be identified but the total field strength is weaker than **A**. This is a graphical illustration of the tradeoff of field strength vs. homogeneity.

#### 4.2.6 Determination of Center Bandwidth Frequencies

Since the  $B_0$  field profile changes for every central magnet displacement, it was necessary to calculate the optimal center bandwidth frequency where the RF coil could be centered to allow calculation of  $S_{max}$  over the region with the highest homogeneity. We chose the magnetic field extrema or where  $\frac{\partial B_0}{\partial y} = 0$  as appropriate frequency values since these points are located in a region of relative homogeneity. Where no local maxima existed, the frequency value was defined where the second spatial derivative of the field was 0 or  $\frac{\partial^2 B_0}{\partial y^2} = 0$ . These points – defined as inflection points – are also representative of a region of relative field uniformity. After defining the evaluation window and center bandwidth frequencies,  $S_{max}$  was integrated in a bandwidth area of  $\pm 100$  KHz. Figure 4.10 A, C indicates center bandwidth values for displacements of -2.2 and -7 mm respectively while Figure 4.10 B, D shows the corresponding bandwidth areas where the maximum signal density was computed.



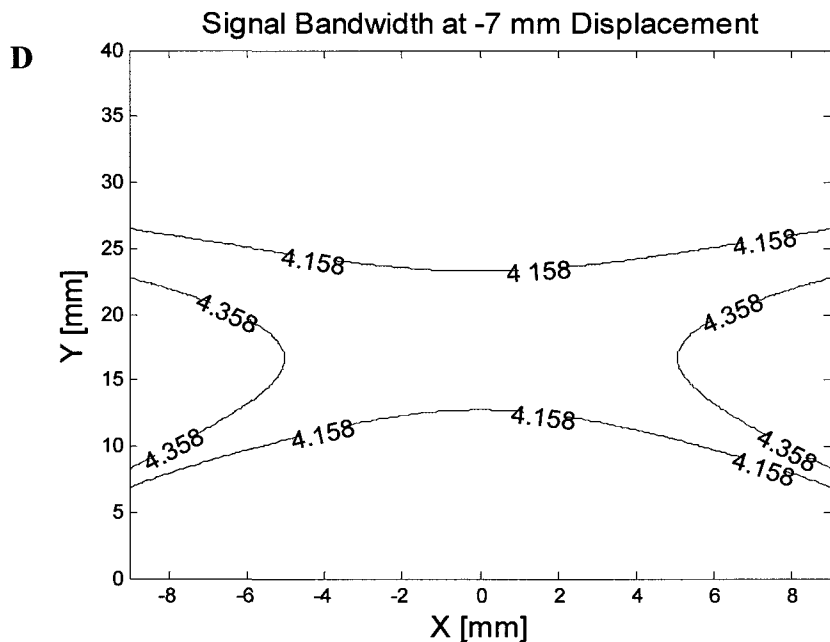
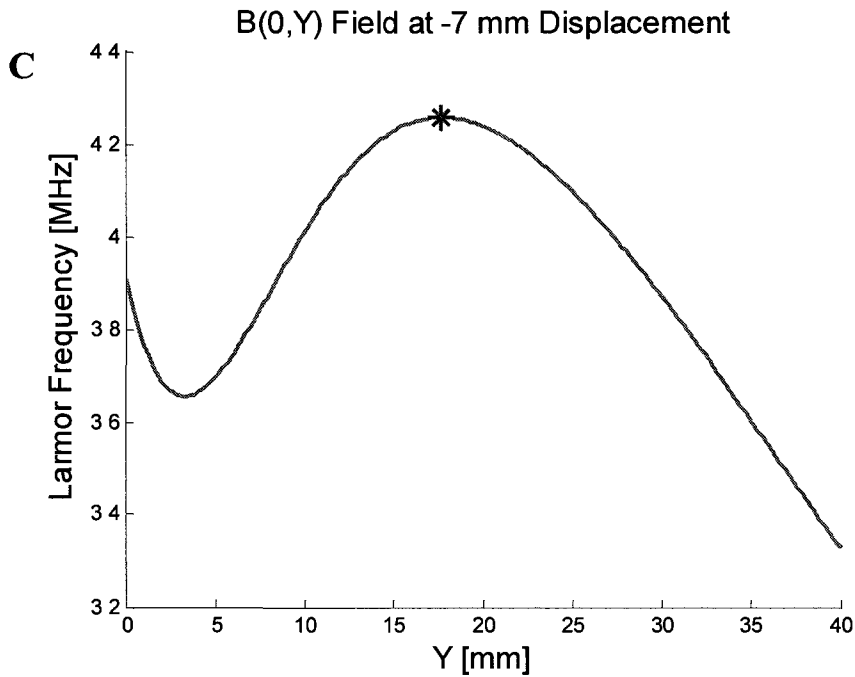


**Figure 4.10.** Center bandwidth values are shown with their corresponding bandwidth area. **A:** At -2 mm displacement a value of approx. 5.2 MHz is noted by the star where the second spatial derivative of the field is 0. **B:** The area between the contour lines corresponds to the bandwidth area in **A**. **C:** At -7 mm displacement, a relatively homogeneous region is noted where a local maxima occurs. **D:** The bandwidth corresponding to **C**. The center bandwidth value of approx 4.2 MHz is lower than **A** but the corresponding bandwidth area in **D** is greater than **C**. These figures illustrate the principle of the tradeoff of field strength vs. homogeneity.

Figure 4.11 shows the center bandwidth frequencies for every displacement where a first or second zeroed field derivative could be calculated.

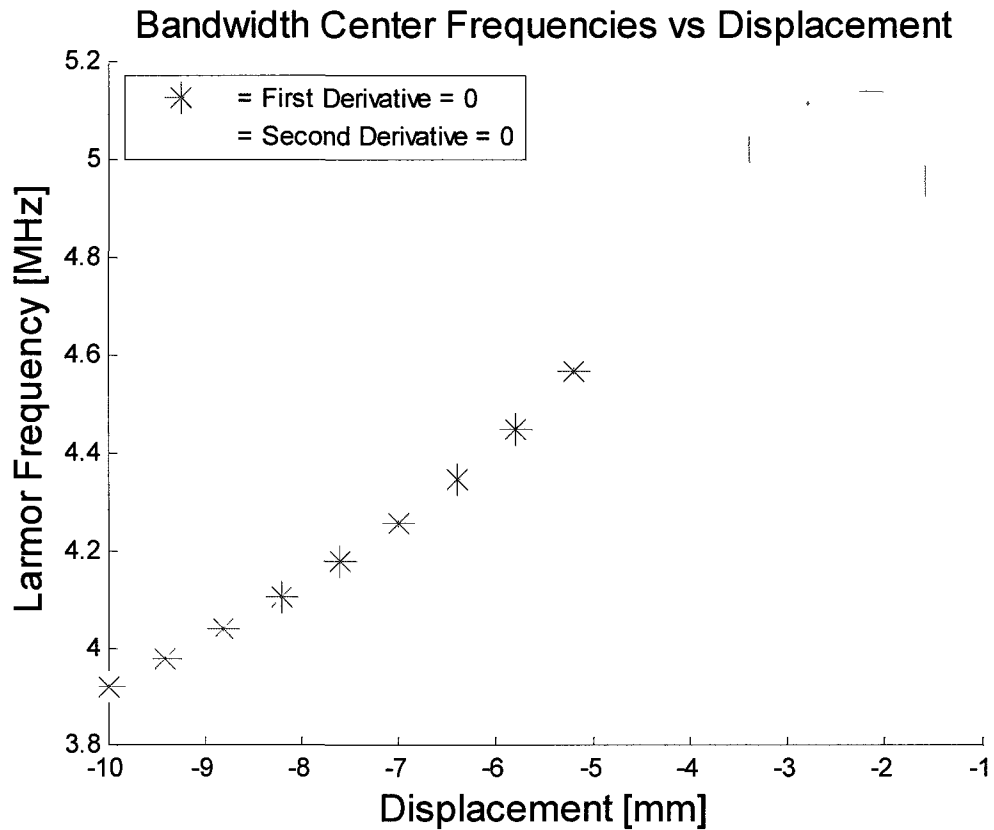
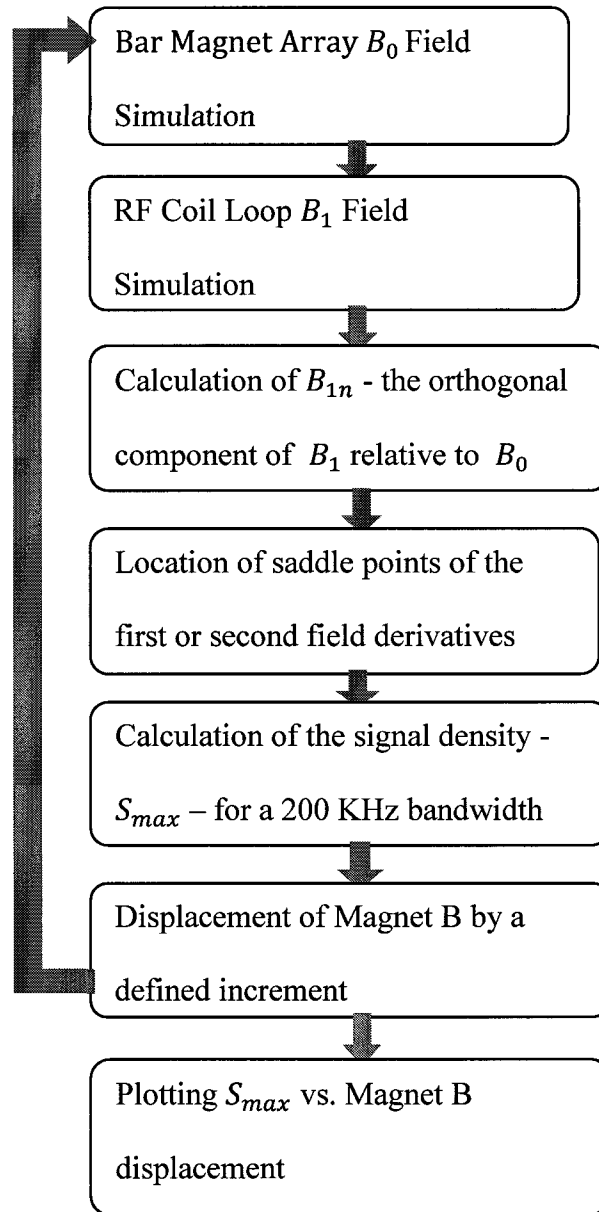


**Figure 4.11.** The center bandwidth frequencies are shown for zeroed first and second order field derivatives vs. central magnet displacements. The decrease in field strength after -2 mm displacement can be attributed to the increasing distance of the zeroed second field derivative from the central magnet surface.

We can note the smooth transition between the first and second derivative points shown in Fig. 4.11. This is due to the fact that at the last point where the first zeroed derivative exists, the second derivative also has a null value. The continuity of the data points seems to validate the choice of the first or second zeroed derivatives as natural regions of homogeneity.

### 4.2.7 Simulation Algorithm Flow

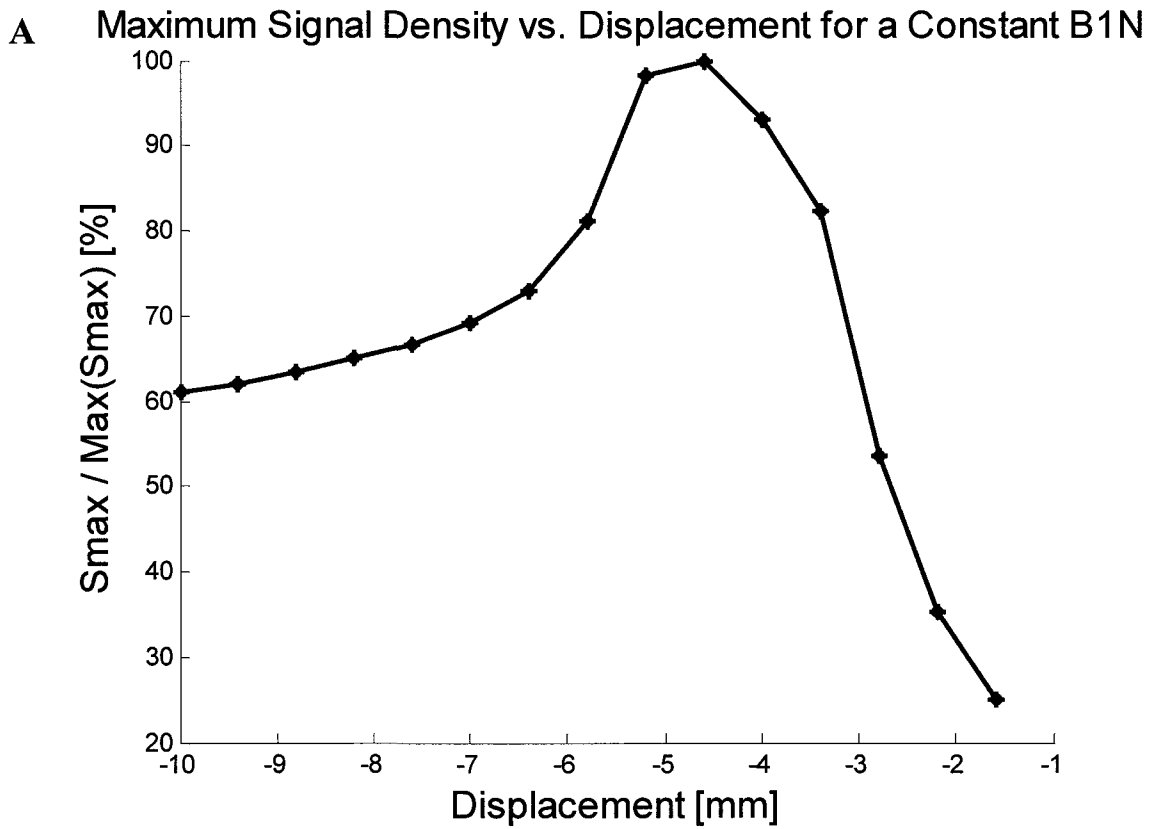
Each of the basic stages of the algorithm used in the signal optimization model discussed in the earlier sections (4.2.1- 4.2.6) is summarized and presented in flow chart form in Figure 4.12.



**Figure 4.12.** The basic stages of the simulation algorithm are; simulation of the  $B_0$ ,  $B_1$ ,  $B_{1n}$  field, calculation of signal density  $S_{max}$  for a 200 KHz bandwidth at saddle points, displacement of central Magnet B and finally plotting  $S_{max}$  vs. Magnet B displacement.

### 4.3 Results

The results of the simulation can be summarized in Figure 4.13 A, B.  $S_{max}$  was calculated for a range of offsets from -10 mm until -1mm for a constant  $B_{1n}$  field in 4.13 A and for a simulated coil centered at the frequency bandwidths in 4.13 B. Although the field strength increases until -2 mm displacement (Figure 4.11), a maximum signal density occurs at approx. -4 mm displacement. At the highest field strength at -2 mm displacement, a dramatic decay of the signal density is noted to approx. 20% of its maximum value. In addition 100% maximum signal density corresponds to a highly homogeneous field or “sweet spot”.



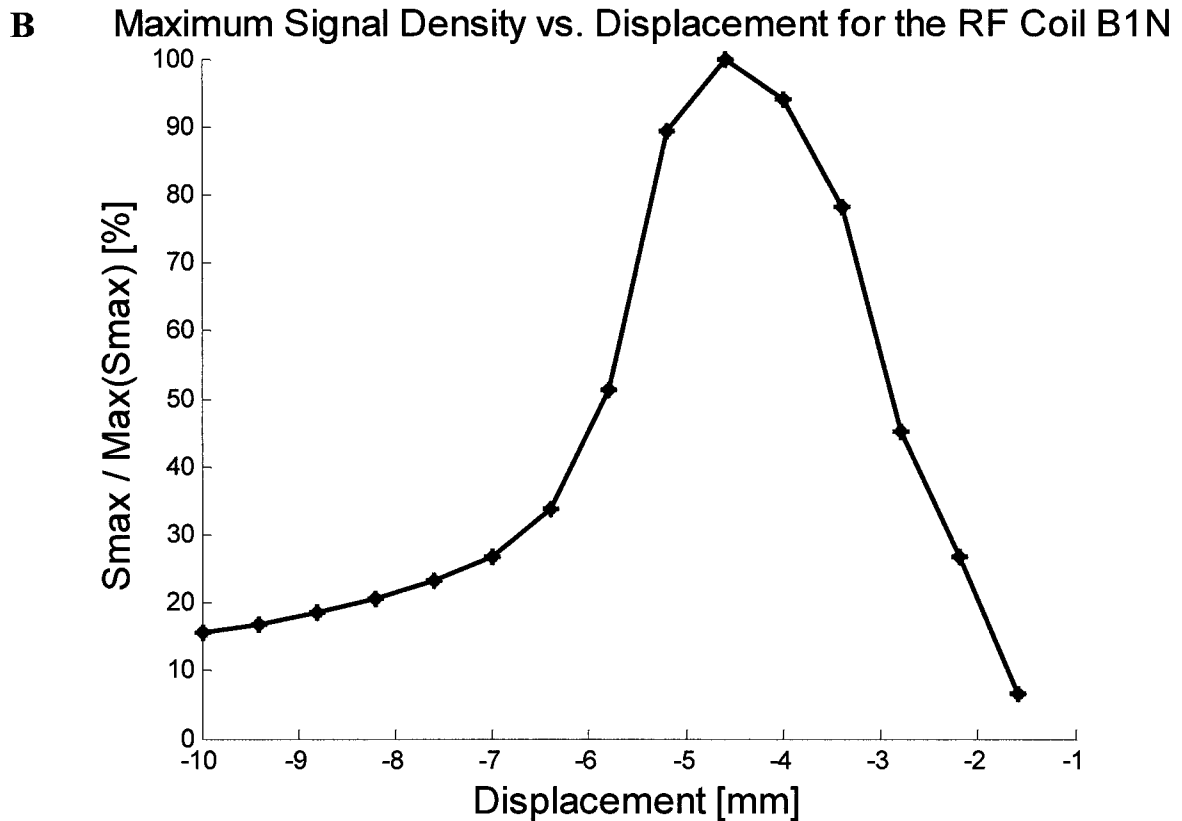


**Figure 4.13.** The percentage of maximum signal density at .6 mm increments is plotted vs. displacement. **A:**  $S_{max}$  was plotted for a constant  $B_{1n}$  with a magnitude of 1 along the y-axis. **B:**  $S_{max}$  was plotted for a RF coil  $B_{1n}$  that varied according to the position of the coil. In both **A** and **B** we can observe a peak at approx. -4 mm – corresponding to the balance of field strength vs. homogeneity that optimizes SNR. The profile of 4.13 **B** is shown to concur with experimental results (See Figure 5.8) Graphs **A** and **B** both indicate that field homogeneity is the dominant factor influencing SNR optimization.

Although differences are noted between 4.13 A and B for offsets less than -4 mm, both graphs show a  $S_{max}$  maximum at approx. -4 mm. Experimental results (Figure 5.8) agree more closely with results derived from an RF coil  $B_{1n}$  field as we would expect.

#### 4.4 Conclusion

Results of the simulation indicate that in this case field homogeneity plays a greater role in SNR optimization than field strength. This simple system is representative of a general case where field cancellation is used to improve homogeneity and thus  $B_0$  decreases as the field homogeneity increases. The implications for unilateral magnet research are that low field highly homogeneous devices may have a higher SNR output than inhomogeneous strong field designs. These simulation results are validated by experimental methods as discussed in chapter 5.

## **5 Experimental Methods**

This chapter is devoted to presenting the experimental methods used to validate the simulation results. An overview of the prototype design, experimental setup, and MR hardware and software specifications is presented. We then describe the components of the experiment such as scanning a 1D field profile, RF coil tuning and signal acquisition. The experimental results are presented and then compared with the simulation graphs.

### **5.1 Prototype Design**

The magnet design used in our experiment described earlier (see 4.1) consists of 3 NdFeB bar magnets contained in a metal housing measuring 10 x 11.5 x 6 cm<sup>3</sup> and weighing approx. 5 kg. The position of the inner magnet can be adjusted with the aid of a mallet to about 1 mm precision. Figure 5.1 illustrates the basic magnet design. The bar magnets are magnetized along the horizontal z-axis (see Figure 4.1).

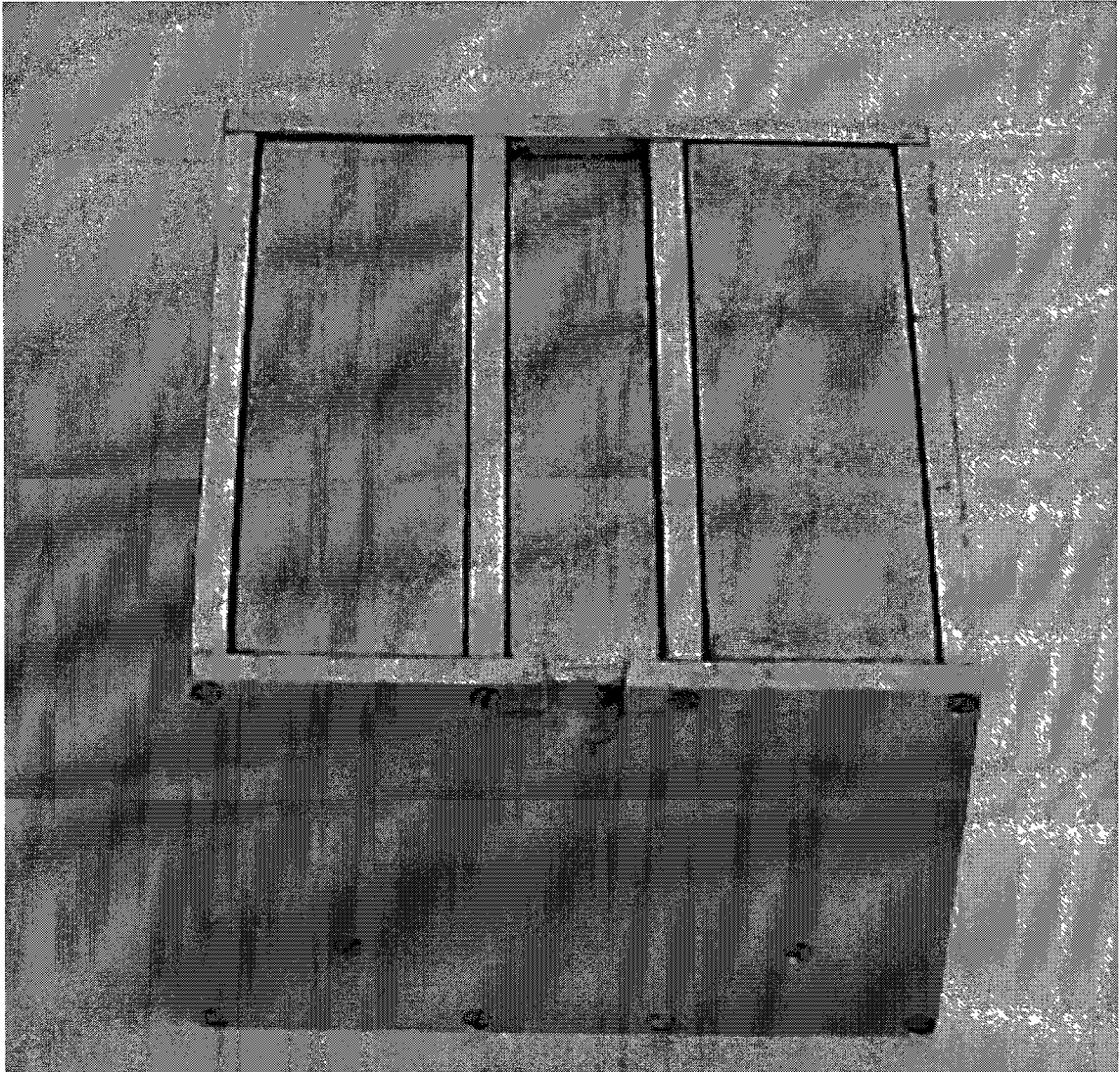


**Figure 5.1** Single-sided magnet array in metal housing. The central adjustable magnet is shown with an offset.

## 5.2 Experimental Design

The sample container consisted of a cylindrical plastic tube of 7.5 cm height and 2 cm diameter. Paraffin oil (Life Brand Baby Oil) was used as a sample due its short  $T_1$  time, slow diffusion and high proton density, allowing fast sensitive measurements. A simple copper wire 2 cm diameter coil loop was wrapped 5 turns around the bottom

centimeter of the sample tube and soldered to a copper conductor .42 cm diameter coaxial cable. After matching and tuning the coil (as described in 5.4.2) the coaxial cable was attached to Bruker Minispec hardware (see 5.3) to allow transmission and reception of precise pulse sequences.

To allow precise movements and stabilization of the sample position, a wooden dowel was wedged into a hole drilled in the container cap after being secured to the Velmex Inc. VXM Stepping Motor Controller 3 -axis positioning system as shown in Figure 5.2.

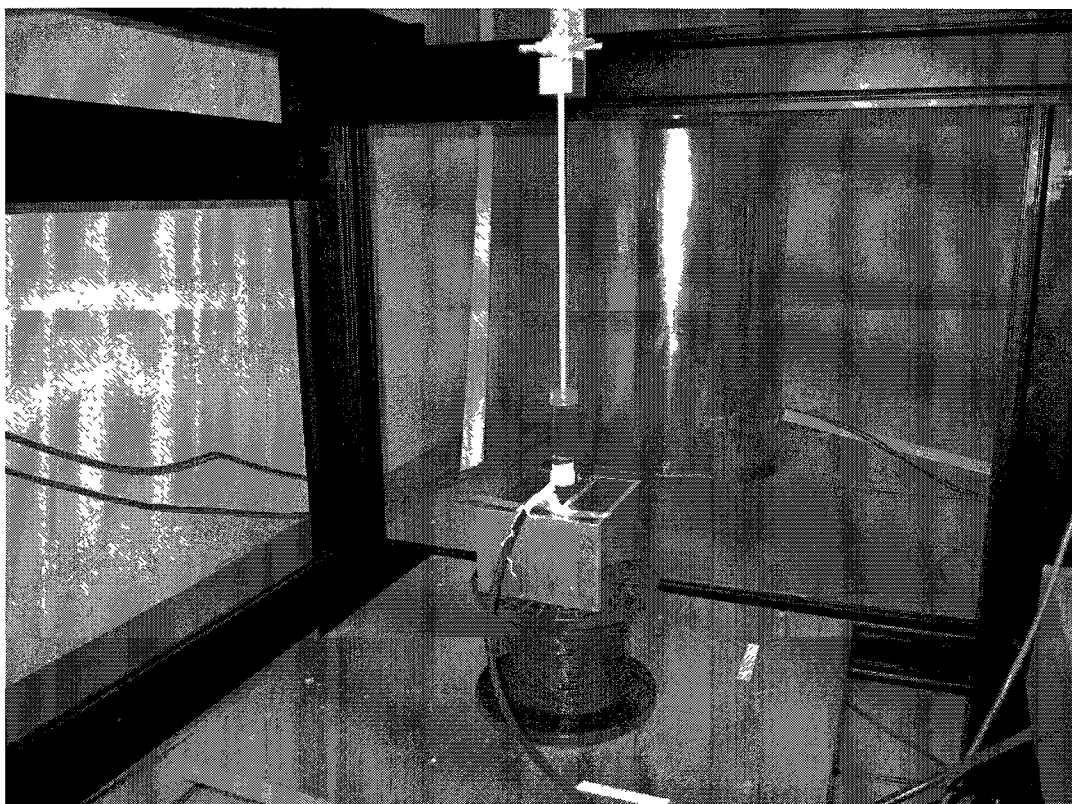


**Figure 5.2** Experimental design: The oil sample is contained in a cylindrical container stabilized above the center of the magnet array by a wooden dowel attached to VXM Stepping Motor Controller. The RF coil soldered to a coaxial cable, is looped around the bottom centimeter of the tube. The spool of wire below the magnet is used for support only and is not part of the NMR measurement.

The VXM stepping motor was controlled by Matlab software for 1D field profile scanning. Adjustments were also made using manual controls.

### 5.3 NMR System Hardware and Software

The Bruker Optics NMR spectrometer was used to control the CPMG pulse sequence used in our experimental work. Pulse sequence parameters and data acquisition and display were controlled by Bruker's ExpSpel Minispec software. The basic hardware components of the system are shown in Figure 5.3.



**Figure 5.3** The Bruker Optics NMR spectrometer hardware includes (right) RF pulse generator and (left – back) a signal preamplifier. Also shown is the (foreground) one-sided magnet array and a Morris Instrument Inc. tuning and matching device.

### 5.3.1 Bruker Minispec Pulse Sequence Parameters

All NMR signal data was generated through a Bruker ExpSpel CPMG application 8 step phase cycle program. The data acquisition parameters modified to generate the pulse sequence were “Scans”- number of NMR signals accumulated before the result is evaluated, “Recycle Delay”- time delay in seconds between multiple scans, “Digital Bandwidth” – digital filter which acts additionally to the analog bandwidth and “Data Acquisition Points” - number of data points acquired per echo. The goal of all the program parameter modifications was to develop the pulse sequence and NMR data processing most appropriate to allow accurate measurements of the transverse magnetization  $M_{xy}$  after application of a  $90^0$  pulse (see 5.3.3 and 5.3.4).

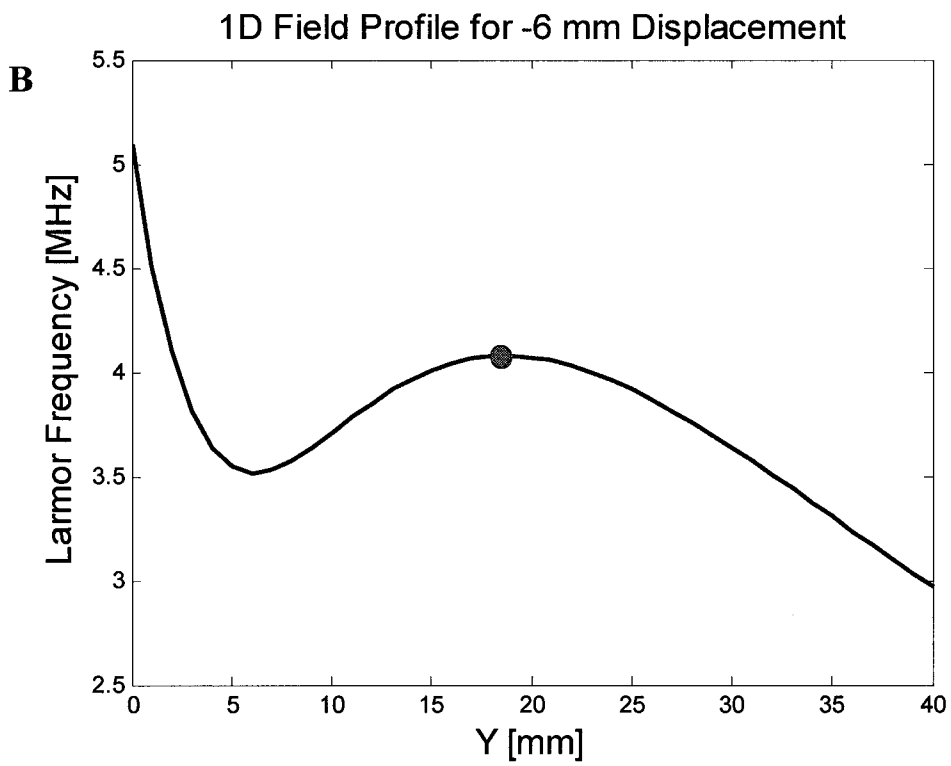
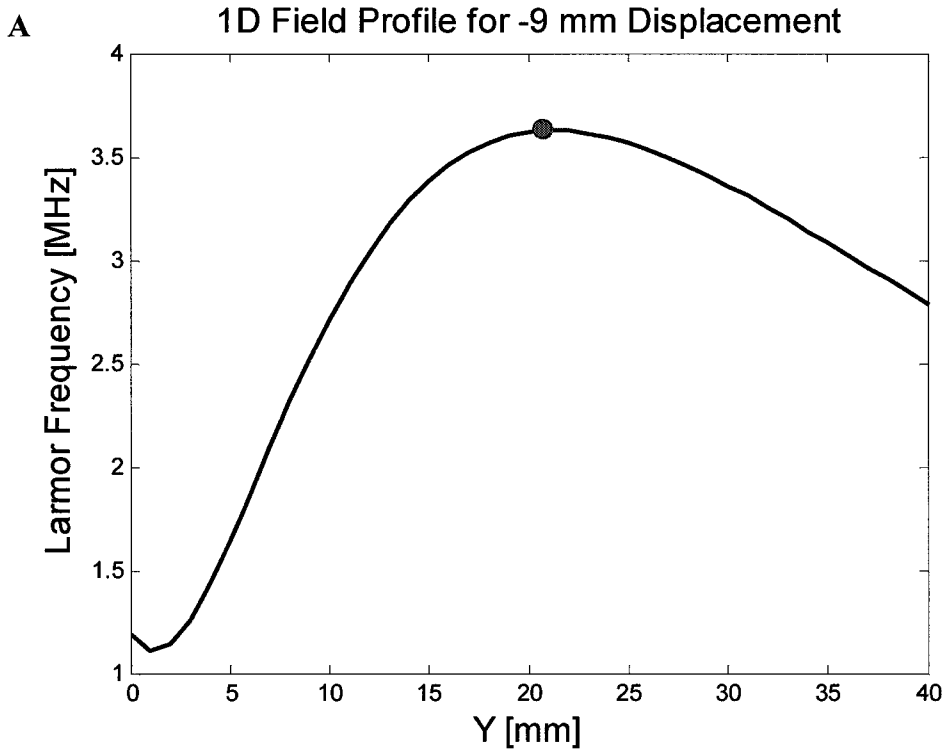
### 5.4 Signal Measurement

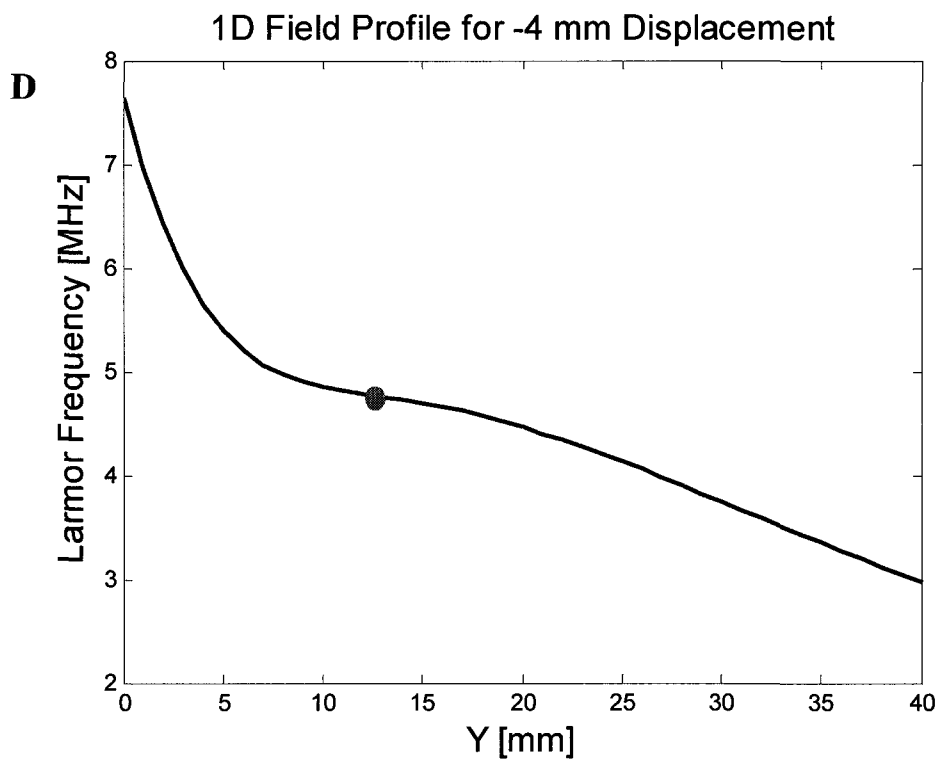
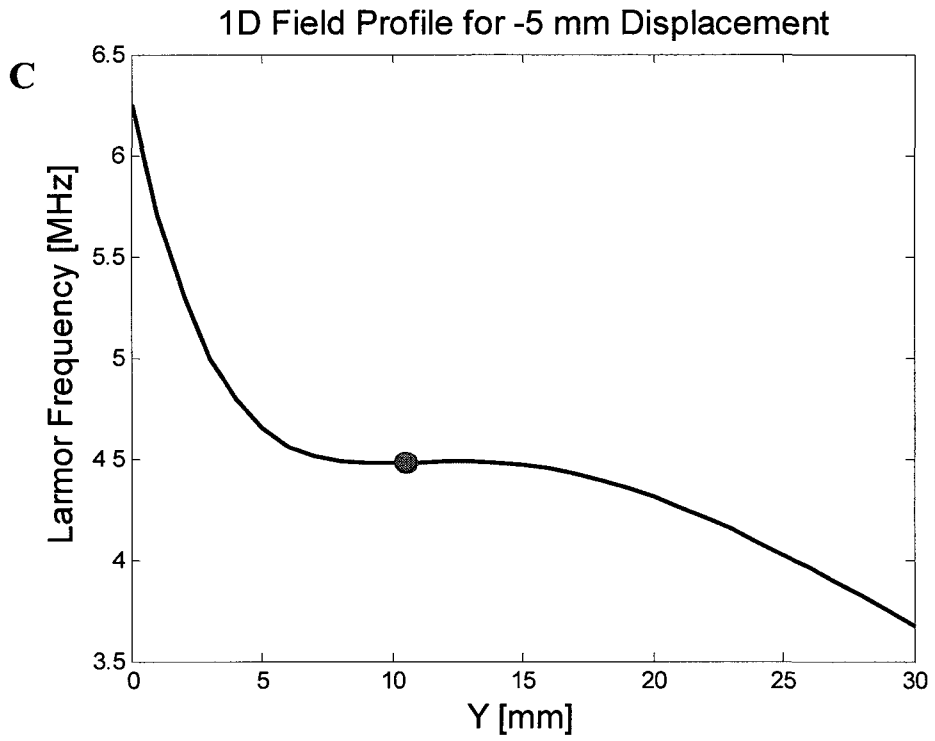
In an attempt to validate the graph of the simulation results in Fig. 4.13, measurements of signal amplitude were taken at 6 different central magnet displacements ranging from -9 to 0 mm. As in the simulation (see 4.2.6) the sample coil was centered at homogeneous regions located for the field profiles for each displacement to increase the signal sensitivity of the measurements.

### 5.4.1 1D Field Scanning

1D  $B_0$  field profiles were obtained for central magnet displacements of -9, -6, -5, -4, -3 and 0 mm. These points were chosen to validate the simulation results shown in Fig. 4.13.

After adjustment to the desired displacement, the magnet was placed under the BiSlide arm of the VXM stepping motor controller. The BiSlide arm was then used to precisely center the probe of a LakeShore 3-Channel Gaussmeter above the magnet array. A Matlab program was used to control vertical movements of BiSlide arm from 0 to 4 cm above the magnet surface with 1 mm increments. Field measurement data in Tesla units was acquired, converted into the resonant frequency for  $^1H$  and plotted as frequency [MHz] vs. displacement [mm]. Homogeneous regions, where the first or second derivatives of the field are equal to zero, were identified visually as the peak of a local maxima or an inflection point between field concavity and convexity. The frequency values at these points were chosen as the center bandwidth frequencies used in the NMR measurements. Figure 5.4 A, B, C, D, E and F shows the plotted field profiles for all experimental displacements.





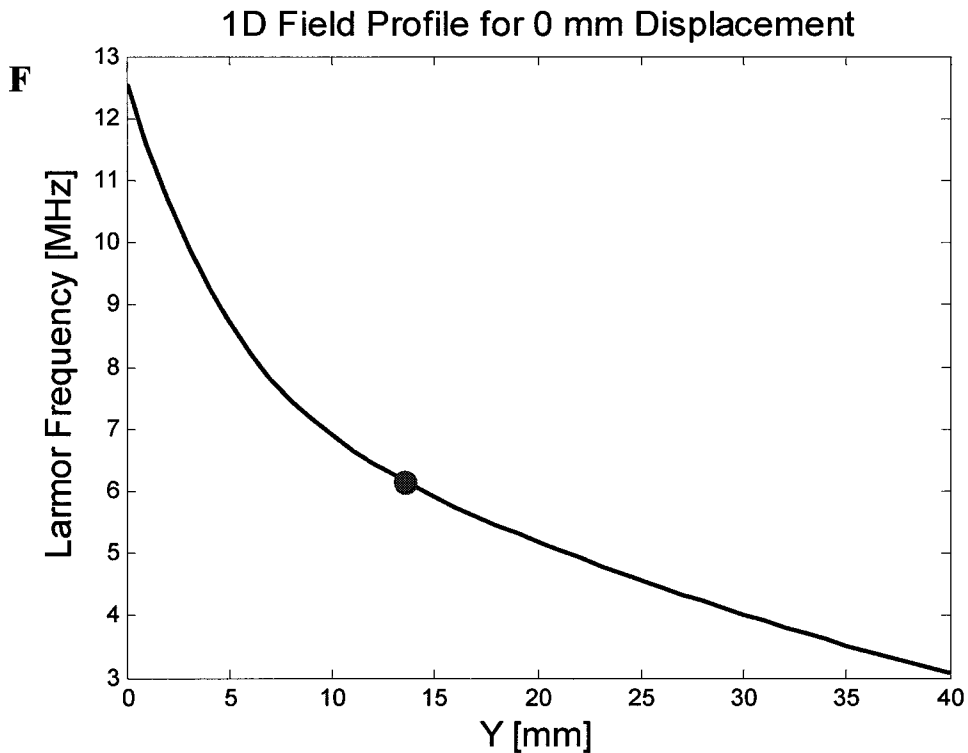
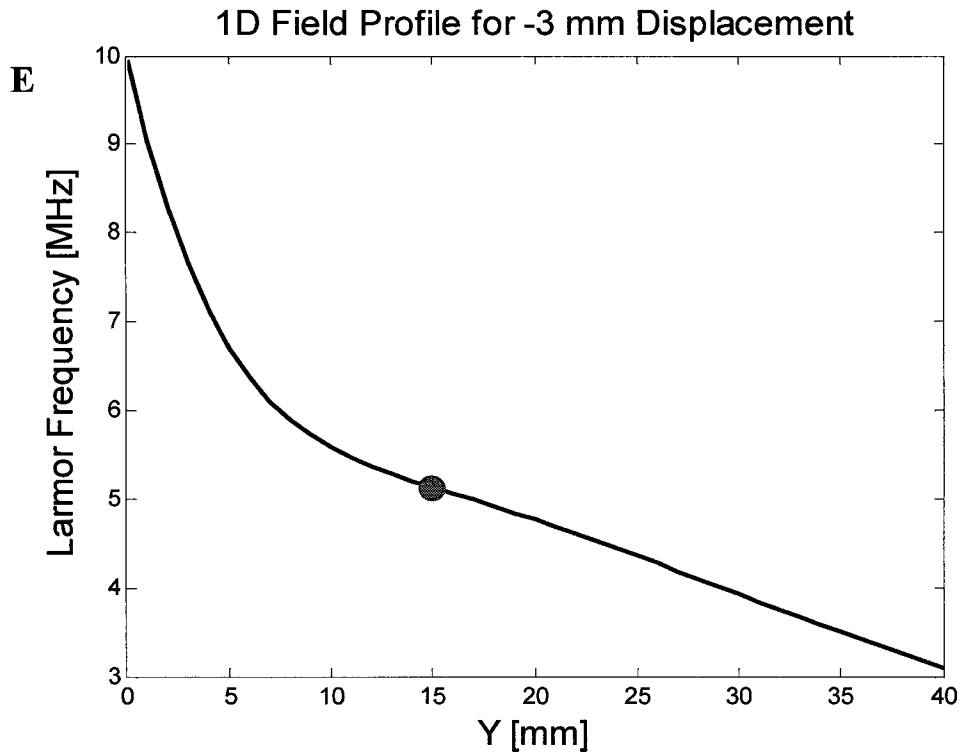


**Figure 5.4** The 1D field profiles of **A** -9 mm , **B** -6mm, **C** -5 mm **D** -4mm **E**-3 mm and **F** 0 mm displacements are shown. Homogeneous regions are indicated by an elliptical marker. We can observe a local maxima for **A-B** whereas for **C-E** no maxima exist and homogeneous points are found at saddle points also known as inflection points. At **F** the graph is shown to monotonically decrease and no maxima or saddle point is found. The homogeneous point was selected as an area of approximate homogeneity at the same distance from the magnet as the -4 mm displacement shown in **D**.

The results presented in Fig. 5.4 A-F are summarized in Table 5.1.

Central Magnet Offset [mm]	Distance of Homogeneous Region from Central Magnet [mm]	Frequency [MHz]
-9	21	3.62
-6	18	4.07
-5	11	4.47
-4	13	4.75
-3	15	5.13
0	13	6.25

**Table 5.1.** A table of homogeneous region location and frequency vs. magnet offsets is presented for results derived from field scanning with a VXM Stepping Motor Controller. We can observe the constant increase of frequency/field strength for progressively less negative displacements. No such clear trend can be observed for homogeneous region distance shown in the second column.

We can observe that the -5 mm offset field profile has the greatest relative region of homogeneity (see Figure 5.4 C). These results agree with experimental data plotted in Fig. 5.8 that shows -5 mm as the point with the greatest measured signal density. In addition we note that no maxima or inflection point was found at 0 mm displacement; rather an approximate homogeneous region was visually selected at the same distance as the -4 mm displacement. This can be compared to our simulated results where homogeneous regions vanish at approx. -1 mm displacement (see Fig. 4.13) and may explain the large discrepancy observed between experimental and theoretical simulation results in Fig 5.6 A, B and Fig. 5.8 that occurs after -2 mm displacement.

For displacements equal or greater than 0 mm an exponential decay of the field profile was noted where no null first or second field derivatives could be found.

#### 5.4.2 RF Coil Tuning and Matching

For every signal amplitude measurement, the RF coil was tuned and matched to the corresponding center bandwidth frequency value to ensure maximum signal sensitivity.

A circuit containing an inductor and a capacitor connected in series or in parallel will resonate at a specific frequency given by [68]

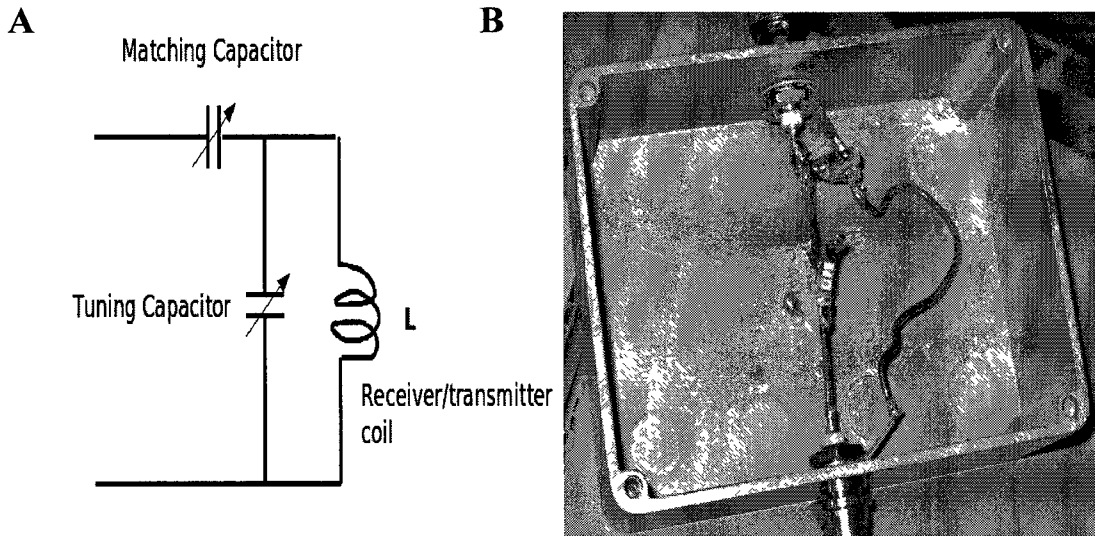
$$\omega_0 = \frac{1}{\sqrt{LC}} \quad 5.1$$

where  $L$  and  $C$  are the coil inductance [H] and capacitance [F] respectively. Since frequency is inversely proportional to capacitance and for progressively less negative displacements an increase in frequency was noted – we started the tuning by adding relatively large amount of capacitors and then removing them for each experiment.

For frequencies beginning at 3.6 MHz until 6.2 MHz or a range of 2.6 MHz we began with a measured total of 4526 pF and concluded our experiments with 646 pF capacitance with a tolerance of  $\pm 5\%$ .

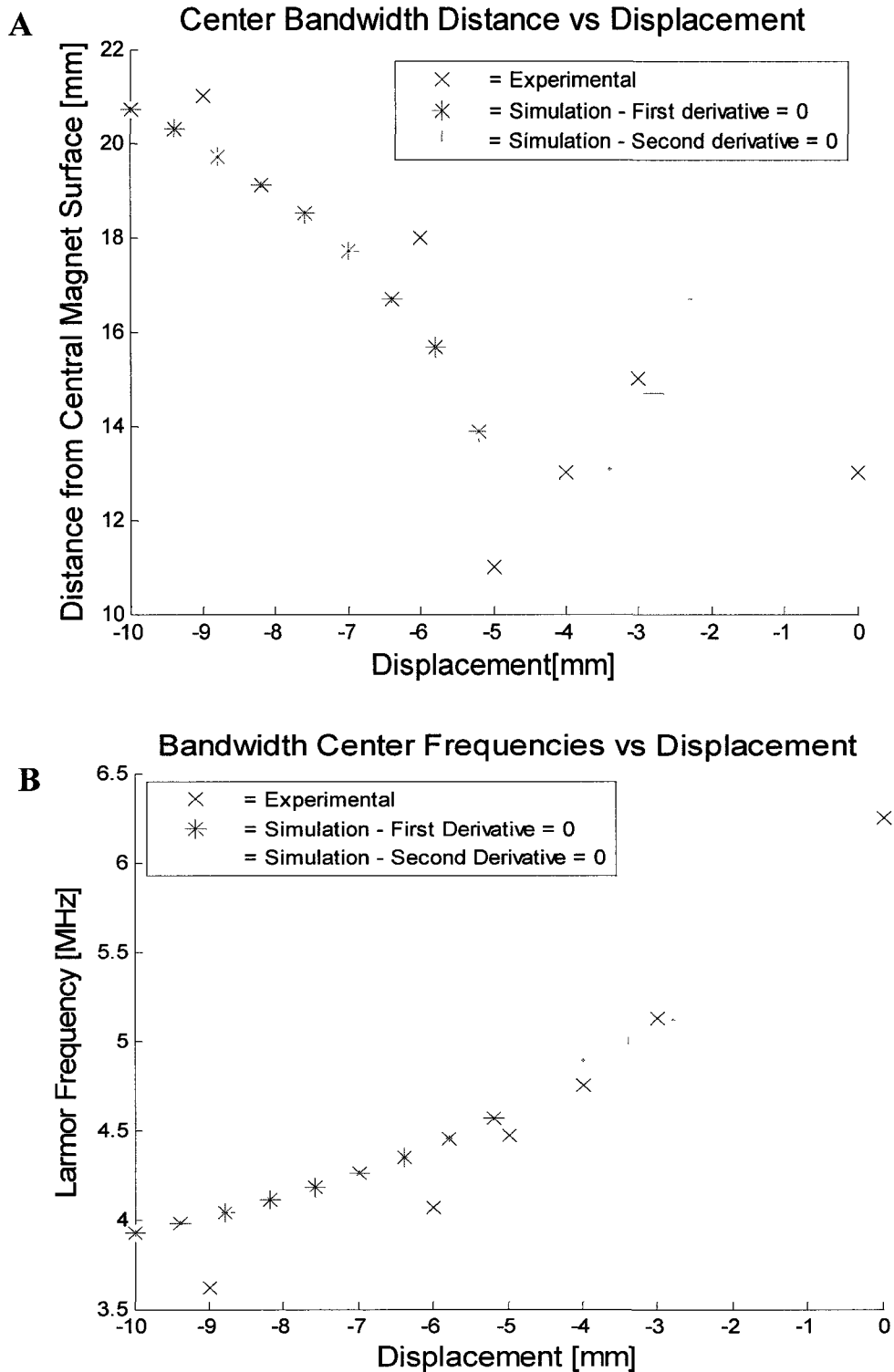
With the aid of a Morris Instrument Inc. Model 405NV+ RF Sweeper device we were able to match the coil to the coaxial cable of  $50 \Omega$  and tune the coil to the center bandwidth values to a precision of  $\pm 25$  KHz.

Figure 5.5 A, B shows a schematic diagram and photograph of the circuit used to tune and match the RF coil.



**Figure 5.5 A.** The resonant circuit consists of an inductance coil and variable capacitors in series and in parallel. Reproduced from [69] **B.** Soldered capacitors in series and in parallel determine the resonant frequency of the circuit.

Figure 5.6 A, B compares experimental vs. simulation results for graphs of bandwidth center frequency vs. displacement and bandwidth center frequency distance from the magnet upper surface vs. displacement. At -2 mm displacement we can note that the simulation results vary widely from the experimental values. This discrepancy can be explained by the simulation method used to identify center value frequencies. Past -2 mm displacement the program identified inflection points at increasing distances from the magnet, resulting in decreased field strength. After approx. -1 mm, no inflection points were identified resulting in the termination of the program. The experimental methods relied on manually identifying homogeneous regions in the field profile resulting in a large variance from simulation results after -2 mm.



**Figure 5.6. A:** A graph of distance of center bandwidth frequencies from the center magnet surface vs. displacement compares simulation and experimental results. **B:** Experimental and simulation results of bandwidth center frequencies vs. displacement. After -3 mm displacement experimental and simulation results from **A** and **B** widely diverge.

We can observe that after -5 mm displacement, the trend of the graph 5.6 A reverses abruptly. This can be explained due to the change of field profile resulting from reducing the negative offset of the central magnet. As the magnet is moved up, the field maxima are lost and homogeneous regions are identified at inflection points. The field profile begins to behave as a decaying exponential function and for each displacement the inflection point moves further way from the magnet eventually reaching a theoretical infinity.

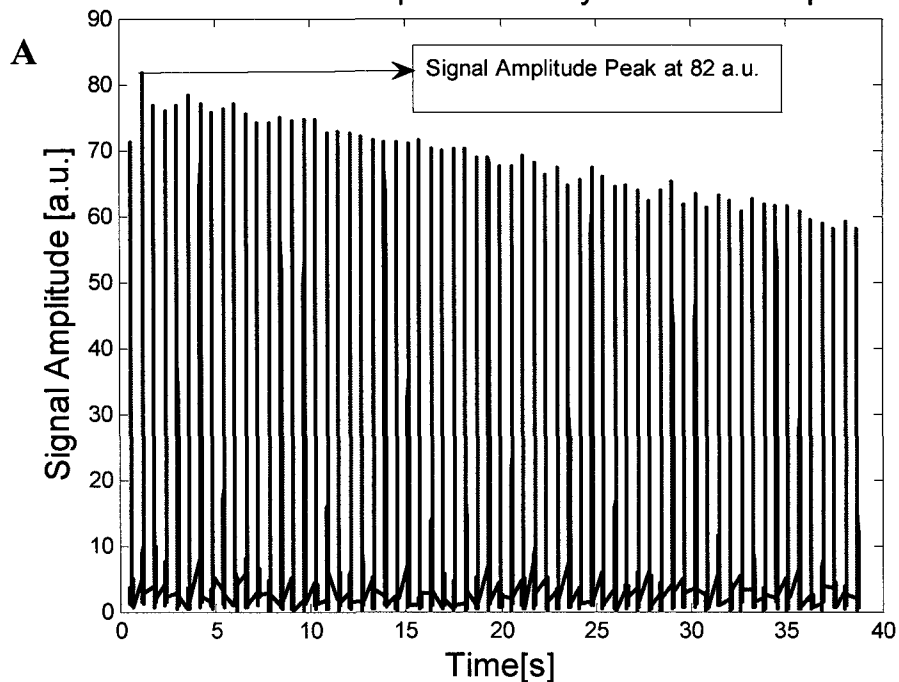
### 5.4.3 CPMG Pulse Sequence

$S_{max}$  can be determined experimentally by measuring the maximum amplitude of the sample transverse magnetization vector  $M_{xy}$ . Theoretically the best method would be to apply a  $90^\circ$  pulse to  $M_0$  and record the peak of the FID. In practice however, the FID of a sample cannot be observed with our system due to its fast decay being of the same order as the dead time of the BrukerMinispec circuits. We therefore decided to utilize the CPMG pulse sequence to refocus the spin system in the transverse plain and to generate a train of echoes. It has been observed that typically the amplitude of the second echo is the largest due to superposition effects of a number of coherence pathways [11]. We decided to measure the amplitude of the second echo of a CPMG train as the best approximation of maximum signal density.

#### 5.4.4 Maximum Signal Amplitude Measurements

The duration of a  $90^\circ$  pulse for each measurement was determined by systematically sweeping the pulse length and observing when a signal maximum was generated. The values were found to range from 6  $\mu\text{s}$  to 4.5  $\mu\text{s}$ . In order to improve the SNR we ran 1024 scans for each measurement. The recycle delay,  $\tau$ , between pulse excitations was set to 0.3 ms since experience indicates that this gives a good tradeoff of SNR vs. time. The digital bandwidth was set to 200 KHz corresponding to the values used in the simulation. A total of 64 echoes were generated with the acquisition time set to .12 ms. 144 data points were acquired per echo in order to generate high resolution echo plots. Figure 5.7 A, B shows absolute plots of a CPMG 64 echo train showing the T2 decay of the oil sample for an offset of  $-5$  and  $-6$  mm respectively. We can note the difference between the poor signal amplitude measured at  $-6$  mm and the high amplitude observed at  $-5$  mm. This indicates the sensitivity of MR measurement to even slight displacements when field homogeneity is greatly altered.

### CPMG 64 Echo Oil Sample T2 Decay for -5 mm Displacement



### CPMG 64 Echo Oil Sample T2 Decay for -6 mm Displacement

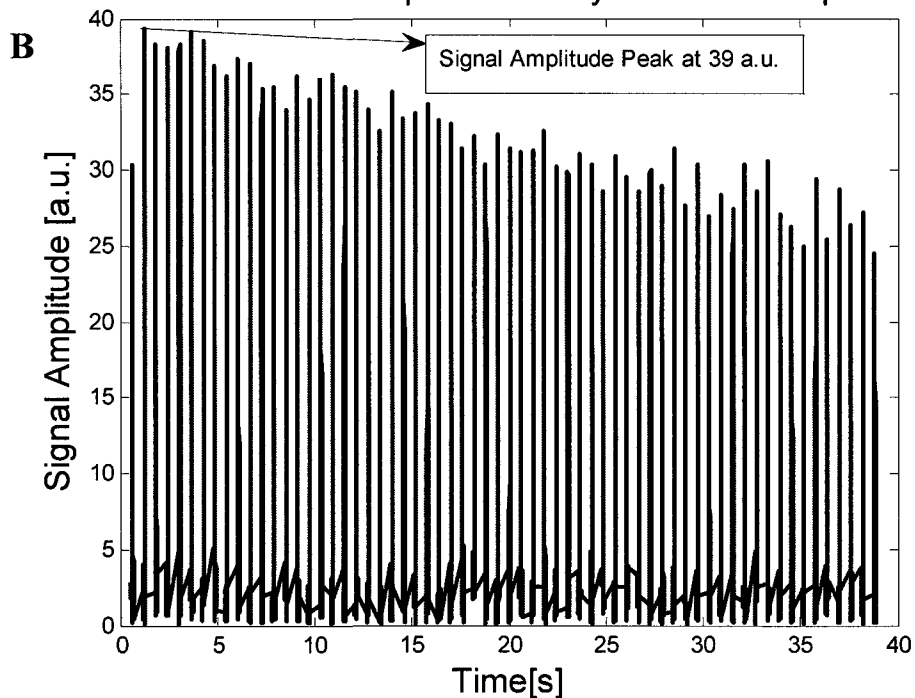


**Figure 5.7.** A plot of the T2 decay of oil for a 64 echo CPMG train **A:** for -5 mm and **B:** -6 mm where each peak represents one echo. The great difference in signal amplitude observed at these 2 points is due to largely changes in field homogeneity. At -5 mm the field profile resembles a plateau, resulting in a large signal amplitude, whereas at -6mm the field profile contains a maxima limiting the field uniformity (see Fig. 5.4 **B, C**)

## 5.5 Results

Figure 5.8 compares the  $S_{max}$  of the simulation to the peak echo amplitudes found experimentally.

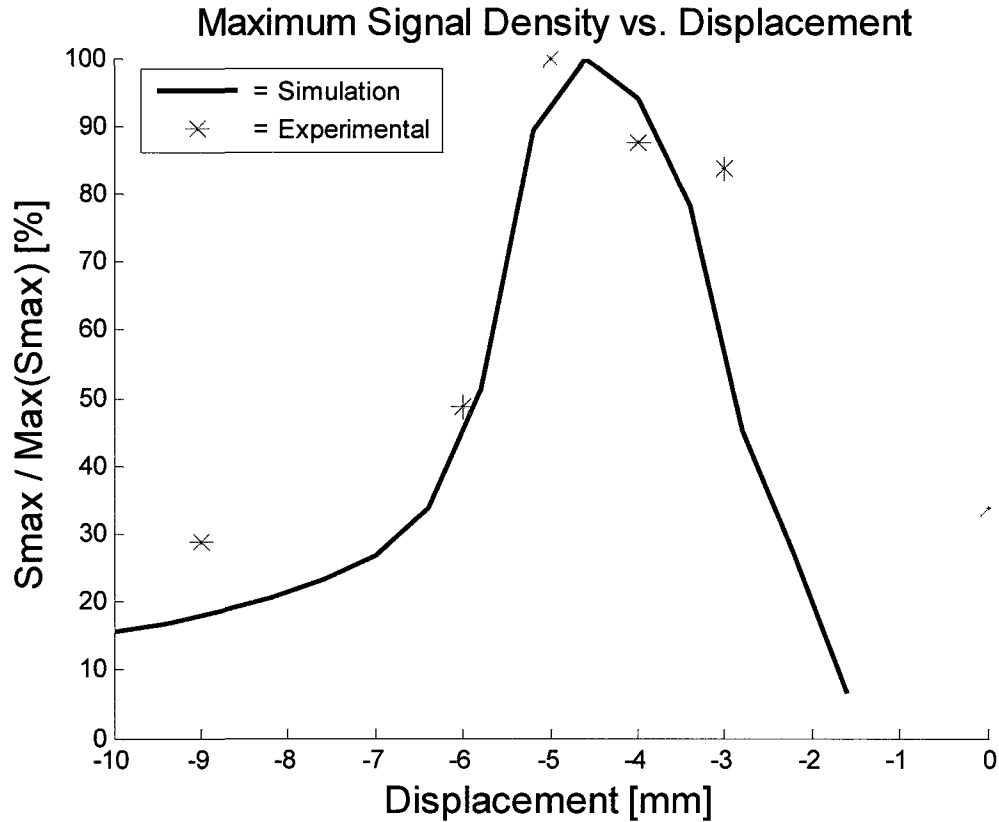


**Figure 5.8.** The simulation and experimental results of maximum signal density vs. displacement are compared. Both the simulation and experimental results were normalized to a maximum value defined as 100%. The simulation is shown as a graph line while the experimental data is plotted discretely.

One of the goals of this work was to observe how SNR is affected by field homogeneity and field strength. Each Matlab image was generated through a matrix of 200x200 or a total of 40 000 discrete grid points. For every central magnet displacement field homogeneity was calculated as the number of points encompassed by the bandwidth contour lines while field strength was calculated as the center bandwidth frequency.

Field homogeneity and strength were normalized and presented as a percentage of the maximum computed value in Figure 5.9.

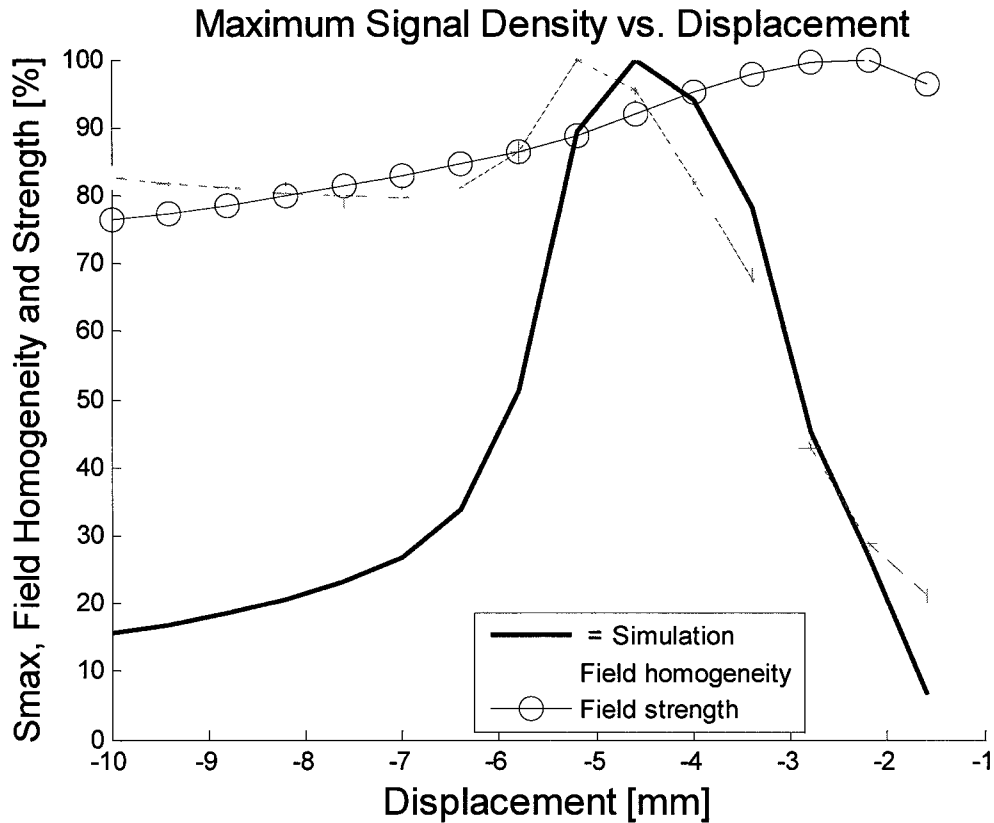


**Figure 5.9** A plot showing maximum signal density, field homogeneity and field strength vs. displacement. Although signal density is dependent on both parameters, field homogeneity is shown to be the dominant factor. A strong correlation between rapidly decaying homogeneity and signal can be noted.

## 5.6 Conclusion

Experimental results have been shown to correlate with simulation findings. The relatively close fit is shown in Figure 5.8. Our results support our simulation methodology of approximating SNR as the integral of  $S_{max}$  within a defined bandwidth.

Figure 5.9 demonstrates the relative influence of field homogeneity and field strength on  $S_{max}$ . We can identify 3 general trends in the graph. From -10 until -7 mm displacement, homogeneity dips and field strength rises resulting in an increase of maximum signal density. From -7 until -5.5 mm, field homogeneity sharply rises and reaches a maximum corresponding to a zone of magnetic “sweet spots”, while field strength continues rising slightly. We can observe a sharp rise in  $S_{max}$  closely following the field homogeneity trend. Although at the peak  $S_{max}$  at -4.5 mm homogeneity has already started to fall off while field strength continues to rise, the close correlation between the former field parameter and  $S_{max}$  show that homogeneity is the dominant factor. After -4.5 mm, a sharp decrease of  $S_{max}$  follows the trend of rapid loss of field homogeneity, again identifying field homogeneity as the primary factor. We can note, however, that for regions of relatively high homogeneity > 80 % and for signal density under 40%, field strength is the dominant factor influencing an increase of  $S_{max}$ . Simulation results indicate that the optimal offset of the central magnet shim unit is approx. -4.5 mm.

## 6 Conclusions and Future Studies

### 6.1 Conclusions

To address the question of the relative influence of field strength and homogeneity on SNR optimization, we simulated a unilateral NMR magnet prototype. Calculation of maximum signal density for a range of simulated shim displacements allowed analysis of the relative weight of field strength vs. homogeneity. To validate simulation findings, we measured the maximum signal amplitude of an oil sample using a CPMG pulse sequence for a range of magnet displacements. Figure 5.8 illustrates the general agreement between the experimental data points and the simulation plots. An analysis of Figure 5.9 demonstrates the close correlation between  $S_{max}$  and field homogeneity, indicating the dominance of the latter over field strength.

We can therefore conclude that overall increasing field homogeneity pays a higher dividend in optimizing SNR performance than raising field strength.

### 6.2 Summary of Contributions

Contributions of this thesis include:

- 2D simulation of one-sided permanent NMR magnet design including a central shim unit and an RF coil,

- development of a relatively simple method of quantifying SNR through computing maximum signal density or  $S_{max}$  over an area defined by a finite bandwidth,
- accurate modeling of maximum signal density measurement for different shim unit configurations,
- development of a novel experimental setup allowing sample NMR measurements to be taken at different distances from the magnet array with high degree of precision and stabilization.

The simulation and experimental work show the greater relative importance of field homogeneity vs. field strength. This may be of importance in determining the future of unilateral NMR magnet design.

### **6.3 Future Work**

The scope of this work can be expanded in a number of directions. Our simulation can be extended to magnet designs with different geometries and spatial dimensions. A 3D model of the laboratory prototype, might allow a more accurate representation of device behavior and performance. To increase signal sensitivity, we measured the sample inside the RF coil, thus negating much of the device flexibility. Future work should implement the simulation algorithm and experimental work on large samples not constrained to the RF coil diameter. More accurate signal measurements would result from an improvement in RF coil design and an easier and more precise method of matching and tuning the resonant circuit.

## References

- [1] Rabi, I. I., Zacharias, J. R., Milman, S. and Kusch, P., "A new Method of Measuring Nuclear Magnetic Moment," *Physical Review* 53(4) (1938) 318.
- [2] Bloch, F., Hansen, W. W. and Packard, Martin., "Nuclear Induction," *Physical Review* 70 (1946) 460-474.
- [3] Purcell, E. M. , Torrey, H. C. and Pound, R. V., "Resonance Absorption by Nuclear Magnetic Moments in a Solid," *Physical Review* 69 (1-2) (1946) 37-38.
- [4] Casanova, F., Perlo, J. and Blumich, B., *Single-Sided NMR*, Springer, Berlin/Heidelberg, 2011, 1-10.
- [5] Mansfield, P. and Grannel, P., "NMR 'diffraction in solids?," *J. Phys. C.* 6 (1973) L422.
- [6] Lauterbur, P., "Image formation by induced local interactions: examples employing nuclear magnetic resonance," *Nature* 242 (1973) 190-191.
- [7] Routley, R. N. and Carlton, K. J., "The HALO system – a light weight portable imaging system," *Journal of Magnetic Resonance Imaging*, 22 (2004) 1145-1151
- [8] Brown, M. A., Semelka, R. C., "Magnetic Resonance Imaging Principles and Applications" in *Computed Body Tomography with MRI Correlation*, Volume 1. Lee, K. T. J., Stuart, S. S., Stanley, J. R. and Heiken, J. P., Lippincott Williams & Wilkins. Philadelphia, PA. 4<sup>th</sup> Ed. 2006.
- [9] Jolesz, F. A., Samset, E., "Clinical Applications of Interventional and Intraoperative MRI" in *Magnetic Resonance Tomography*. Reiser, M. F., Semmler, W. and Hricak, H., Springer-Verlag. Berlin Germany. 2008.

- [10] Chang, W. -H., Chen, J.-H. and Hwang, L.-P., "Single-sided mobile NMR with a Halbach magnet," *Magnetic Resonance Imaging* 24 (2006) 1095-1102.
- [11] Casanova, F., Perlo, J., "NMR in Inhomogeneous Fields," in: *Single-Sided NMR*. Springer, Casanova, F., Perlo, F. and Blumich, B., Berlin/Heidelberg, 2011, 11-56.
- [12] Manz, B., Coy, A., Dykstra, R., Eccles, C. D., Hunter, M. W., Parkinson, B. J. and Callaghan, P. T., "A mobile one-sided NMR sensor with a homogeneous magnetic field: The NMR-MOLE," *Journal of Magnetic Resonance* 183 (2006) 25-31.
- [13] Brix, G., "Physical Basics," in: *Magnetic Resonance Tomography*. Reiser, M. F., Semmler, W. and Hricak, H., Eds. Berlin Heidelberg: Springer-Verlag, 2008, 8-9.
- [14] Rajan, S. S., "MRI A Conceptual Overview," New York, NY: Springer-Verlag, 1997, 1-11.
- [15] Rahman, A. and Choudhary, M. I., "The Basics of Modern NMR Spectroscopy," in: *Solving Problems with NMR Spectroscopy*. San Diego, California: Academic Press, Inc. 1996, 1-89.
- [16] Duer, M. J., "Introduction to solid-state NMR spectroscopy," Cornwall, Great Britain, Blackwell Publishing Ltd. 2004, 4.
- [17] Buxton, B. R., "Introduction to functional magnetic resonance imaging: principles and techniques," New York, NY, Cambridge University Press, 2002.
- [18] Brown, M. A. and Semelka, C. R., "MRI basic Principles and Applications," 4<sup>th</sup> Ed. Hoboken, New Jersey: John Wiley & Sons, 2010
- [19] Hahn, E. L., "Spin Echoes," *Phys. Rev.* 80 (1950) 580-594.
- [20] Carr, H. Y. and Purcell, E. M., "Effects of diffusion on free precession in nuclear magnetic resonance experiments," *Phys. Rev.* 94(3) (1954) 630-638.

- [21] Meiboom, S. and Gill, D., "Modified spin-echo method for measuring nuclear relaxation times," *Rev. Sci. Instrum.* 29 (8) (1958) 699-691.
- [22] Le Bec, G., Yonnet, J-P. and Raoof, K., "Development of a small NMR probe," *Journal of Magnetism and Magnetic Materials*, 316 (2007) 240-243.
- [23] Blumich, B., *NMR Imaging of Materials*. Oxford Science Publications. New York, NY. 2000.
- [24] Liang, Z. P., Lauterbur, P. C., *Principles of Magnetic Resonance Imaging*. IEEE Press, New York, NY (2000).
- [25] Lipton, M. L., "Totally Accessible MRI, A User's Guide to Principles, Technology, and Applications". Springer Science + Business Media, LLC. New York, NY. 2008.
- [26] Felder, J., "Spectrometer Hardware," in: *Single-Sided NMR*. Springer, Casanova, F., Perlo, F. and Blumich, B., Berlin/Heidelberg, 2011, 221-240.
- [27] Blumich, B., Perlo, J., and Casanova, F., "Mobile single-sided NMR," *Progress in Nuclear Magnetic Resonance Spectroscopy*, 52 (2008) 197-269.
- [28] Perlo, J., Casanova, F. and Blumich, B., "Ex situ NMR in highly homogenous fields:  $^1\text{H}$  spectroscopy," *Science* 315 (2007) 1110-1112.
- [29] Goga, N. O., Pirnau, A., Szabo, L., Smeets, R., Riediger, D., Cozar, O. and Blumich, B., "Mobile NMR: Applications to Materials and Biomedicine," *Journal of Optoelectronics and Advanced Materials* 8(4) (2006) 1430-1434.
- [30] Solis, S. E., Cuellar, G., Wang, R. L., Tomasi, D. and Rodriguez, A. O., "Transceiver 4-leg birdcage for high field MRI: knee imaging," *Revista Mexicana De Física*. 54 (3) (2008) 215-221.

- [31] Bock, M., "Technical Components" in Magnetic Resonance Tomography. Reiser, M. F., Semmler, W. and Hricak, H., Springer-Verlag. Berlin Germany. 2008.
- [32] Brown, R. J. S., and Gamson, B.W., "Nuclear Magnetism Logging," Petroleum Transactions, 219 (1960) 199-207.
- [33] Perlo, J., "Magnets and Coils for Single-Sided NMR," in: Single-Sided NMR. Springer, Casanova, F., Perlo, F. and Blumich, B., Berlin/Heidelberg, 2011, 99.
- [34] Anferova, S., Anferov, V., Adams. M., Blumler, P., Routley, N., Hailu, K., Kupferschlager, K., Mallet, M. J. D., Schroeder, G., Sharma, S. and Blumich, B., "Construction of a NMR-MOUSE with Short Dead Time," Concepts in Magnetic Resonance, 15 (1) (2002) 15-25.
- [35] Cooper, R. K., and Jackson, J. A., "Remote (Inside-Out) NMR. Remote Production of a Region of Homogeneous Magnetic Field," Journal of Magnetic Resonance, 41 (1980) 400-405.
- [36] Clow. H., Percival. W. S. and Walters. P. E., US. Patent 4.629 986. 1986.
- [37] Prammer, G. P., "NUMAR (1991-2000)," Concepts in Magnetic Resonance, 13(6) (2001) 389-395.
- [38] Kleinberg, R. L., "NMR Well Logging at Schlumberger," Concepts in Magnetic Resonance, 13(6) (2001) 396-403.
- [39] Miller, M. N., "Part 3: NUMAR and NUMALOG," Concepts in Magnetic Resonance, 13(6) (2001) 379-385.
- [40] Kleinberg, R. L., Sezginer, A., Griffin, D. D. and Fukuhara, M., "Novel NMR Apparatus for Investigating an External Sample," Journal of Magnetic Resonance, 97 (1992) 466-485.

- [41] Nicholls, C. I., and Delosantos, A., "Hydrogen transient nuclear-magnetic-resonance for industrial moisture sensing," *Drying Technol.* 9(4) (1991) 849-873.
- [42] Paetzold, R. F., Matzkanin, G. A., and Delosantos, A., "Surface soil-water content measurement using pulsed nuclear magnetic-resonance techniques," *Soil Sci. Soc. Am. J.* 51(2) (1985) 537-540.
- [43] Matzkanin, G. A., "Review of Nuclear Magnetic Resonance for Nondestructively Characterizing Materials," in: *Nondestructive Characterization of Materials XI*. Springer, Green, R. E., Djordjevic, B. B. and Hentschel, M. P., Berlin, 1989. 793-800.
- [44] Danieli, E. P., "High-Resolution Spectroscopy in Highly Homogeneous Stray Fields," in: *Single-Sided NMR*. Springer, Casanova, F., Perlo, F. and Blumich, B., Berlin/Heidelberg, 2011, 165-186.
- [45] Chang, W. -H., Chen, J.-H. and Hwang, L.-P., "Single-sided mobile NMR apparatus using the transverse flux of a single permanent magnet," *Magnetic Resonance Imaging* 28 (2010) 129-138.
- [46] Perlo, J., Casanova, F. and Blumich, B., "Single-sided sensor for high-resolution NMR spectroscopy," *Journal of Magnetic Resonance* 180 (2006) 274-279.
- [47] Marble, E. A., Mastikhin, I. V., Colpitts, B. G. and Balcom, B. J., "A Compact permanent magnet array with a remote homogeneous field," *Journal of Magnetic Resonance* 186 (2007) 100-104.
- [48] Pulyer, Y. M. and Patz, S., "US patent 5572132, MRI probe for external imaging," 1996.
- [49] Goelman, G., Prammer, MG., "The CPMG pulse sequence in strong magnetic-field gradients with applications to oil-well logging," *Journal of Magnetic Resonance Ser. A*

113(1) (1995) 11-18.

[50] McDonald, P. J., "Stray Field Magnetic Resonance Imaging," *Prog. Nucl. Magn. Reson. Spectrosc.* 30 (1997) 69-99.

[51] Sagawa, M., Fujimura, Yamamoto, Y. M., "Permanent magnet materials based on the rare earth-iron-boron tetragonal compounds," *IEEE Trans. Magn. MAG-20* (5) (1984) 1584-1589.

[52] G. Eidmann, R. Savelsberg, P. Blumler, and B. Blumich, "The NMR MOUSE, a MOBILE Universal Surface Explorer," *J. Magn. Res., Series A*, vol. 122, pp. 104-109, 1996.

[53] Hugon, C., Aguiar, P. M., Aubert, G., and Sakellariou, D., "Design, fabrication and evaluation of a low-cost homogeneous portable permanent magnet for NMR and MRI," *C. R. Chimie*, 13 (2010) 388-393.

[54] Blumich, B. and Casanova, F., "Mobile NMR," in: *Modern Magnetic Resonance*. Vol. 1-3. Webb, G. A., Dordrecht, 2006, 369-378.

[55] Marble, E. A., "Magnets for Unilateral Magnetic Resonance," Ph.D. Dissertation, Dept. Elect. Eng., University of New Brunswick, New Brunswick, CA, 2007. 34.

[56] Zimmer, G., Guthausen, A. and Blumich, B., "Characterization of technical elastomers by the NMR-MOUSE ]," *Solid State Nucl. Magn. Resonan.* 12 (1998) 183-190.

[57] Martin, D. R., Ablett, S., Pedersen, H. T. and Mallet, M. J. D., "The NMR mouse: its applications to food science," *Magn. Resona. Food Sci. Latest Dev.* 286 (2003) 54-61.

[58] Sharma, S., Casanova, F., Wache, W., Segre, A. and Blumich, B., "Analysis of historical porous building materials by the NMR-mouse," *Magn. Reson. Imaging*

21(2003) 204-209.

[59] Blumich, B., Anferov, V., Anferova, S., Klein, M., Fechete, M., Adams, M. and Casanova, F., "Simple NMR-MOUSE with a Bar Magnet," *Concepts Magn. Resonan.* 15B (2002) 255-261.

[60] A.E. Marble, "Strong, Stray Static Magnetic Fields", *IEEE Trans. Magn.* vol. 44, no. 5 (2008) 579.

[61] Abragam, A., *Principles of nuclear magnetism.* Oxford University Press. New York, NY. 1994.

[62] Hoult, D. I., Richards, R. E., "Signal-to noise ratio of nuclear magnetic resonance experiment," *J. Magn. Reson.* 24(1) (1976) 71-85.

[63] M. D. Hurlimann, D.D. Griffins, "Spin Dynamics of Carr-Purcell\_Meiboom\_Gill-like Sequences in Grossly Inhomogeneous B<sub>0</sub> and B<sub>1</sub> Fields and Application to NMR Well logging," *J. Magn. Reson.* 143 (2000) 121

[64] Balibanu, F., Hailu, K., Eymael, R., Demco, D. E. and Blumich, B., "Nuclear Magnetic Resonance in Inhomogeneous Magnetic Fields," *J. Mag. Reson.* 145 (2000) 246-258.

[65] W.R. Smythe, *Static and Dynamic Electricity*, McGraw-Hill, New York, 1950 , 266.

[66] "Elliptic Integrals – Table of Available Elliptic Integrals", [http://mymathlib.webtrellis.net/functions/elliptic\\_integrals.html](http://mymathlib.webtrellis.net/functions/elliptic_integrals.html), May 2 2011

[67] Veliyun, E., Mastikhin, I. V., Marble, E. A. and Balcom, B. J., "Rapid determination of the fat content in packaged dairy products by unilateral NMR," *J. Sci. Food Agric.* 88 (2008) 2563-2567.

[68] Horowitz, P., Hill, Winfield., The art of electronics. Cambridge University Press. New York, NY. 2<sup>nd</sup> Ed. 1989.

[69] How an NMR Probe Works. [Online]. Retrieved July 8<sup>th</sup> 2011 from <http://chem4823.usask.ca/nmr/probe.ht>

[70] Fukushima, E. and Roeder, S. B. W. “Experimental NMR A Nuts and Bolts Approach”, Reading, MA: Addison-Wesley, 1981.

[71] Kuperman, V. “Magnetic Resonance Imaging Physical Principles and Applications”, Academic Press, San Diego, 2000.